Fully quantum state-resolved inelastic scattering of NO(X) + Kr: differential cross sections and product rotational alignment

M. Brouard,[1, a)] H. Chadwick,[1, b)] S. D. S. Gordon,[1] B. Hornung,[1, c)] B. Nichols,[1] J. Kłos,[2, d)] F. J. Aoiz,[3, e)] and S. Stolte[4, f)]

[1)] *The Department of Chemistry, University of Oxford, The Physical and Theoretical Chemistry Laboratory, South Parks Road, Oxford, OX1 3QZ, United Kingdom.*

[2)] *Department of Chemistry and Biochemistry, University of Maryland, College Park, MD, 20742, USA.*

[3)] *Departamento de Química Física, Facultad de Química, Universidad Complutense, 28040 Madrid, Spain*

[4)] *Institute of Atomic and Molecular Physics, Jilin University, Changchun 130012, China.*[g)]

(Dated: 22 September 2014)

Fully quantum state selected and resolved inelastic scattering of NO(X) by krypton has been investigated. Initial Λ-doublet state selection is achieved using an inhomogeneous hexapole electric field. Differential cross sections and even-moment polarization dependent differential cross sections have been obtained at a collision energy of 514 cm^{-1} for both spin-orbit and parity conserving and changing collisions. Experimental results are compared with those obtained from quantum scattering calculations and are shown to be in very good agreement. Hard shell quantum scattering calculations, are also performed, to determine the effects of the different parts of the potential on the scattering dynamics. Comparisons are also made with the NO(X) + Ar system.

[a)]Electronic mail: mark.brouard@chem.ox.ac.uk

[b)]Current address: Laboratoire de Chimie Physique Moléculaire, Ecole Polytechnique Fédérale de Lausanne, Lausanne, Switzerland

[c)]Current address: School of Chemistry, University of Bristol, Cantock's Close, Bristol, BS8 1TS, UK

[d)]Electronic mail: jklos@umd.edu

[e)]Electronic mail: aoiz@quim.ucm.es

[f)]Electronic mail: stolte@chem.vu.nl

[g)]Department of Physics and Astronomy, LaserLaB, Vrije Universiteit, Amsterdam, De Boelelaan 1081, 1081 HV Amsterdam, The Netherlands, and Laboratoire Francis Perrin, Bâtiment 522, DRECEM/SPAM/CEA Saclay, 91191 Gif sur Yvette, France

I. INTRODUCTION

Collisions of open shell species have been the subject of much investigation as a result of their importance in a diverse range of fields, such as atmospheric, astrophysical, and combustion chemistry. The nitric oxide (NO) molecule has an unpaired electron in its ground electronic state, so exhibits the complex dynamics of open-shell molecules, yet it is relatively unreactive, and is thus convenient to study experimentally. For these reasons it has become a prototype for investigating the inelastic scattering of open shell molecules.

The unpaired electron in NO(X) resides in a π^* orbital, giving rise to two spin-orbit levels, the $^2\Pi_{\frac{3}{2}}$ lying approximately $123\,\mathrm{cm}^{-1}$ above the ground $^2\Pi_{\frac{1}{2}}$ state. Within each spin-orbit manifold, there is a ladder of rotational levels, each of which is split into two near degenerate Λ-doublet levels, denoted f ($\epsilon = -1$) and e ($\epsilon = 1$), which for $j = 0.5$ are nearly degenerate and differ only in total NO parity [$p = \epsilon(-1)^{j-1/2}$].

During the course of a collision, either spin-orbit manifold can be populated, leading to scattering taking place on two coupled potential energy surfaces. On non-linear approach of a Kr atom to the NO(X) molecule, the degeneracy of the $^2\Pi$ state is lifted, resulting in two potential energy surfaces of A' and A'' symmetry. For Hunds case (a) molecules, Alexander[1,2] has shown that the spin-orbit conserving transitions can be considered to take place on a summed potential:

$$V_{\mathrm{sum}}(R,\gamma) = \frac{1}{2}[V_{A'}(R,\gamma) + V_{A''}(R,\gamma)], \tag{1}$$

whilst spin-orbit changing collisions are coupled by a difference potential:

$$V_{\mathrm{diff}}(R,\gamma) = \frac{1}{2}[V_{A'}(R,\gamma) - V_{A''}(R,\gamma)]. \tag{2}$$

Here, $V_{A'}$ and $V_{A''}$ are the two lowest lying potential energy surfaces of the NO(X) + Kr system. The $V_{A'}$ surface is associated with the orbital containing the unpaired electron lying in the triatomic plane, whereas $V_{A''}$ corresponds to the orbital being perpendicular to the plane. R is the distance between the centre of mass of the NO molecule and the Kr atom and γ is the angle between $\boldsymbol{R}$ and the NO bond axis, $\boldsymbol{r}$.

Despite this complexity, it is still possible to perform full quantum mechanical scattering calculations on NO(X) plus the rare gases. Furthermore, a number of accurate potential energy surface have been determined for these systems,[3–7] and as such they have been the focus of numerous experimental[8–30] and theoretical[31–34] investigations.

On collision of NO(X) with a rare gas atom, the total NO parity can either be conserved or changed, depending on the Λ-doublet level before and after the collision. In order to fully elucidate the effect of parity on the scattering dynamics, it is necessary to select only a single Λ-doublet level prior to the collision, and probe a single Λ-doublet level after collision. Initial state selection can be achieved using an inhomogeneous hexapole electric field, whereas final state selection is possible using (1+1′) resonantly enhanced multiphoton ionization (REMPI), or other spectroscopic detection techniques. Using such methods, parity dependent effects have been found in both the integral[20] and differential cross sections (DCSs)[24–26,28] for several NO–rare gas systems. Parity dependent oscillations were observed in the DCSs of the NO(X) + Ne[28] and Ar[26,27,35] systems, which were attributed to interference between trajectories sampling different regions of the potential.[26,27] Such oscillations were not observed experimentally in the NO(X) + He system at 508 cm^{-1} [24] as the de Broglie wavelength is much longer due to the smaller reduced mass. 'Parity pairs', in which adjacent final states with the same parity (those with the same value of $n = j' + \epsilon'/2$, for example, $j' = 8.5, f$ and $j' = 7.5, e$) exhibit similarly structured DCSs, were observed in all three systems.

Further experimental and theoretical studies have investigated the collision-induced alignment (CIA) and orientation (CIO) of the product rotational angular momentum in the NO(X) + He,[21] Ne,[22,23] and Ar[9,10,12,29,36,37] systems. This measurement represents a triple vector correlation between the initial and final relative velocities, $\boldsymbol{k}$ and $\boldsymbol{k}'$, and the rotational angular momentum of the scattered NO(X), $\boldsymbol{j}'$, and is characterized by the polarisation dependent differential cross sections (PDDCSs), $\rho_{q\pm}^{\{k\}}(\theta)$ of rank k and component q. Such high order vector correlations provide valuable insight into the dynamics of the collision. The collision-induced alignment in all three systems was found to be well explained by the simple kinematic apse model. The NO(X) + Kr system has received much less attention; Marinakis *et al.*[38] calculated the CC QM $\rho_0^{\{2\}}(\theta)$ PDDCSs for the NO(X) + Kr system and observed parity pair behavior similar to that found for the DCSs, although this has yet to be confirmed experimentally. Despite the many similarities between the NO(X) + Ar and Kr systems, differences in the range, well depths, and anisotropy of the potential energy surfaces, together with a modest change in the de Broglie wavelength, arising from the different reduced masses, make NO(X) + Kr an interesting system for study.

In this paper we present experimental DCSs and PDDCSs for spin-orbit conserving and

changing collisions of NO(X) + Kr at a collision energy of 514 cm^{-1} with full Λ-doublet resolution of both the initial and final states. The outline of the paper is as follows; first a summary of the experimental methods used in this work will be given in Section II. This Section also briefly describes the method of data analysis by which the experimental DCSs and PDDCSs are extracted from the experimental images, including a modification to previous methods to account for the depolarisation of slow moving molecules. Section II concludes with the details of the calculations presented in this work. In Section III A and III B the spin-orbit conserving and changing experimental and theoretical images and DCSs are presented and discussed. The experimental collision-induced alignment results are then compared with theoretical calculations in III C, again for both spin-orbit conserving and changing collisions. A comparison with the NO(X) + Ar system in Section III D highlights the similarities and differences between the two systems and compares full close coupled quantum mechanical calculations with quantum mechanical hard-shell and kinematic apse model results to yield further insight into the dynamics of both systems.

II. METHODS

A. Experimental Methods

The crossed molecular beam experiment, which combines hexapole state selection and a $(1 + 1')$ REMPI scheme coupled with velocity mapped[39] ion imaging[40] to allow complete quantum state selection, has been described in detail elsewhere,[26,29] so only a brief summary will be given here. The primary beam of NO molecules (16 % NO in Ar) is generated using a General valve pulsed at 10 Hz, which is then doubly skimmed and state selected using a hexapole electric field.[26] The hexapole state selector focusses only NO molecules in the $|\Omega = 0.5, j' = 0.5, f\rangle$, odd parity, low field seeking state. The focussed NO(X) molecules are then intersected perpendicularly by the skimmed secondary beam consisting of neat Kr. In order to have confidence that cluster formation was not significant in this beam, a series of images were recorded whilst varying the backing pressure of Kr. No effect was found on the observed DCS and a backing pressure of 3 bar was used, as in previous experiments.[26,28]

The secondary beam is pulsed on for two shots, then off for two, to allow background subtraction on a shot-by-shot basis, minimizing any systematic errors due to laser power

drift or such like. The output of a XeCl excimer laser ($\lambda = 308\,\mathrm{nm}$) is split, with 90% used to pump a tunable dye laser (Coumarin 450) which lases at 452 nm. The output is frequency doubled to produce radiation at $\approx 226\,\mathrm{nm}$ which can be tuned to the NO(A $\leftarrow$ X) rotational transition of choice, with the remaining 10% of the 308 nm output used to ionize the NO(A) molecules. The excitation laser is directed through a Rochon polarizer then a photoelastic modulator (PEM), which allows the linear polarisation to be flipped from horizontal (H) to vertical (V) (with respect to the plane defined by the molecular beams) on alternate shots. On entering the scattering chamber the lasers intersect each other perpendicularly, and the molecular beams at 45° in a coplanar fashion.

The resulting NO^+ ions are extracted using velocity map[39] ion imaging[40] using a standard three electrode arrangement and detected using a pair of matched MCPs and a P43 phosphor screen. The flashes on the phosphor are recorded using a CCD camera and transferred to a computer for processing. On average each image was acquired for 20,000 laser shots for the DCSs and 200,000 laser shots for the CIA data. The latter are obtained from normalized difference images, $(I_\mathrm{V} - I_\mathrm{H})/(I_\mathrm{V} + I_\mathrm{H})$, where I_H and I_V refer to images obtained with horizontally and vertically polarized light, respectively. Because the CIA data are displayed as the normalized difference signal, a much larger number of shots is required to converge the image.

The NO(X) beam velocity was determined to be $625\,\mathrm{ms}^{-1}$ (as in previous experimental studies[26–28]) and the Kr beam $408\,\mathrm{ms}^{-1}$, leading to a centre of mass collision energy of $514\,\mathrm{cm}^{-1}$ with a full-width-at-half-maximum of $50\,\mathrm{cm}^{-1}$, which was confirmed by analysing the size of the ion images with varying j'. The collision energy calibration was achieved by looking at the radius of the ion images as a function of j', as described fully in Ref. 27. Note that, at this collision energy, the maximum energetically accessible NO(X) rotational state for spin-orbit conserving transitions is $j' = 17.5$, whilst for spin-orbit changing collisions the maximum rotational state is $j' = 14.5$.

B. Data Analysis

The method of data analysis for both the DCS and CIA images has been discussed in detail previously,[26–29] so only the relevant details will be given here. The detection

probability of a single scattering event, n, is given by the expression:[29]

$$I(x_n, y_n) = u(x_n, y_n)\, P_{\mathrm{scatt}}(\theta_n)\, P_{\mathrm{V/H}}(\theta_n; \Gamma^n_{\mathrm{V/H}}), \tag{3}$$

where $u(x_n, y_n)$ is the apparatus function[29] for a pixel of position (x_n, y_n) on the detector, $P_{\mathrm{scatt}}(\theta_n)$ is the angular scattering distribution (proportional to the DCS), and $P_{\mathrm{V/H}}$ is the polarisation dependent transition probability. The Euler angles, $\Gamma^n_{\mathrm{V/H}}$, can be determined from the relative orientation of the collision frame (defined by $\boldsymbol{k}$ and $\boldsymbol{k'}$) and the laser frame (defined by the electric vector of the light, and the direction of probe laser propagation).[29] The polarisation dependent transition probability is then expressed in terms of the renormalized PDDCSs:

$$P_{\mathrm{V/H}}(\theta_n; \Gamma^n_{\mathrm{V/H}}) = 1 + \sum_{kq} \rho^{\{k\}}_{q\pm}(\theta_n) F^{\{k\}}_{q\pm}(\Gamma^n_{\mathrm{V/H}}). \tag{4}$$

The $F^{\{k\}}_{q\pm}(\Gamma^n_{\mathrm{V/H}})$ functions are defined in Ref. 29 and contain the geometric information needed to calculate the contribution of a particular PDDCS. Note that the first term in Eq. (4), when substituted into Eq. (3), corresponds to the probability of detecting a single scattering event without polarisation, and is that which is required to determine the DCS.

Previous studies that have looked at the collision-induced alignment for NO(X) + Ar collisions have found that either the alignment is underestimated,[12] or that there is a slight asymmetry in the experimental normalized difference images, $(I_{\mathrm{V}} - I_{\mathrm{H}})/(I_{\mathrm{V}} + I_{\mathrm{H}})$.[29] In the current work, a similar asymmetry can be seen in the experimental images, as shown in Fig. 1, and it appears that this effect is most evident at around $j' = 13.5$. Wade *et al.*[12] suggested that this discrepancy could be due to depolarisation of molecules that remain in the detection volume for longer times. The Newton diagram for the collision is shown in the right panel of Fig. 1 and superimposed onto the two experimental images for $j' = 6.5$ and $j' = 13.5$. In the case of $j' = 13.5$, the Newton sphere almost intersects the lab frame zero velocity, so the slowest molecules are travelling at only about $8\,\mathrm{ms}^{-1}$ and so will remain in the detection volume for hundreds of microseconds and thus experience significant depolarisation. At $j' = 6.5$, the slowest molecules are still travelling at approximately $170\,\mathrm{ms}^{-1}$ and therefore leave the detection volume much faster and so are much less depolarized.

Molecules which are slow moving in the laboratory could be depolarised as a result of the interaction of NO with the earth's magnetic field, as suggested by Wade *et al.*[12] However, in the present experiments this seems unlikely because the interaction volume was screened

by μ-metal shielding. Collisions of translationally cold NO molecules with Kr atoms or NO molecules in the molecular beam gas pulses, or with other cold NO molecules in the low lab velocity portion of the Newton sphere, might also cause collisional depolarization, and we believe such processes are likely to be the dominant mechanism in the current experiments. To account for this depolarisation, Eq. (4) can be modified according to:

$$P_{\mathrm{V/H}}(\theta_n;\Gamma^n_{\mathrm{V/H}}) = 1 + \left[\sum_{kq} \rho^{\{k\}}_{q\pm}(\theta_n) F^{\{k\}}_{q\pm}(\Gamma^n_{\mathrm{V/H}})\right] \times \mathrm{e}^{-\beta t_{\mathrm{det}}}\,, \tag{5}$$

where t_{det} is the time at which the scattered NO(X) is detected. The constant β will dictate how easily the molecule is depolarized and will depend on many factors, such as the depolarisation cross section, the lab frame velocity of the molecule, and the position within the molecular beam. Whilst it is not possible to calculate this accurately, a typical value was chosen such that after approximately 100 μs in the detection volume, 50% of the molecules were depolarized, which is broadly consistent with the known molecular beam properties, and the known rotational energy transfer and elastic collisional depolarization cross sections for NO(X) + Ar, and other related systems.[41–43] Some variation in β with final rotational state was allowed for, reflecting the relatively modest dependence of elastic depolarization cross sections on quantum state.[41]

Using the modified polarisation dependent detection probability, Eq. (3) can be summed over many trajectories to build up a simulation of the experimental image, sampling the initial starting conditions as described in Ref. 27. To fit the experimental images to obtain the DCSs, the intensity of the experimental image was written as a sum of basis functions:[27,28]

$$I_{\mathrm{exp}}(x,y) = \sum_l \frac{2l+1}{2} a_l B_l(x,y)\,, \tag{6}$$

where the basis functions are defined

$$B_l(x,y) = \sum_n u(x_n,y_n)\, P_{\mathrm{V/H}}(\theta_n;\Gamma^n_{\mathrm{V/H}})\, P_l(\cos\theta_n)\,, \tag{7}$$

i.e. the product of the instrument function and the polarisation dependent transition probability, weighted by the l^{th} Legendre polynomial $[P_l(\cos\theta_n)]$ to account for the angular distribution of the scattered product. The expansion coefficients of the DCS, a_l, were then optimized by fitting the experimental image in Fourier moment space using a genetic algorithm.[26–28,44] The fitted DCS is then be given by

$$P_{\mathrm{scatt}}(\theta) = \sum_l \frac{2l+1}{2} a_l P_l(\cos\theta)\,. \tag{8}$$

Similar procedures were used to obtain the renormalized PDDCSs, $\rho_0^{\{2\}}(\theta)$ and $\rho_{2+}^{\{2\}}(\theta)$, from the normalized difference images, $(I_{\rm V} - I_{\rm H})/(I_{\rm V} + I_{\rm H})$, as has been fully described in Ref. 29. We have shown elsewhere that the experiment is insensitive to the $\rho_{1+}^{\{2\}}(\theta)$ renormalized PDDCS.[29]

Simulations of the experimental ion images were performed using the same basis functions as for in the fitting of the experimental images, but employing the theoretical angular distributions and polarization moments presented in the following Sections. Further details about the simulation procedures are described elsewhere.[29]

C. Calculation Details

The experimentally determined DCSs and PDDCSs will be compared with those obtained from close-coupled quantum mechanical (CC QM) scattering calculations performed using the HIBRIDON suite of codes[45,46] on the $V_{\rm sum}$ and $V_{\rm diff}$ potential energy surfaces of Wen *et al.*[4] These PESs were calculated at the restricted coupled cluster level including single, double and perturbational triple excitations with the augmented, correlation consistent, triple-zeta basis set quality with extra bond-functions placed in the mid-distance between Kr and the center-of-mass of NO.[4] The dynamics calculations were run over a grid of collision energies from $485\,{\rm cm}^{-1}$ to $545\,{\rm cm}^{-1}$ with a spacing of $15\,{\rm cm}^{-1}$, and the theoretical DCSs were weighted over the experimental collision energy distribution. A propagation from 4.5 bohr to 60 bohr was used, with a rotational basis up to $j = 20.5$ and partial waves up to $J = 160$ were needed to converge the calculations. Calculations for the NO(X) + Ar system were performed as described previously[26,36] at a collision energy of $530\,{\rm cm}^{-1}$ and employed the CCSDT potential energy surfaces of Alexander.[3,47]

The normalized polarization dependent differential cross sections (PDDCSs), $P_q^{(k)}(\theta)$, characterize the polarization of the angular momentum of the scattered particles as a function of scattering angle. Quantum mechanically, these can be calculated via:[48,49]

$$P_q^{(k)}(\theta) = \frac{2\pi}{\sigma}\,\frac{1}{4k^2}\,\frac{1}{2j+1}\sum_{m,m_1',m_2'} f_{jm\Omega,\epsilon\to j'm_1'\Omega'\epsilon'}(\theta) f^*_{jm\Omega\epsilon\to j'm_2',\Omega'\epsilon'}(\theta)\langle j'm_1', kq|j'm_2'\rangle \qquad (9)$$

where k is the modulus of the relative wavenumber vector, σ is the integral cross section for the specific $j\Omega\epsilon \to j', \Omega'\epsilon'$ transition, $\langle j'm_1', kq|j'm_2'\rangle$ is a Clebsch Gordan coefficient, and $f_{jm\Omega,\epsilon\to j'm'\Omega'\epsilon'}(\theta)$ is the scattering amplitude for the transition with the indicated quantum

number. The renormalized PDDCSs, $\rho_q^{(k)}(\theta)$, are calculated according to:[48]

$$\rho_q^{(k)}(\theta) = \frac{P_q^{(k)}(\theta)}{P_0^{(0)}(\theta)} \tag{10}$$

where $P_0^{(0)}(\theta) = (2\pi/\sigma)\mathrm{d}\sigma/\mathrm{d}\omega$ is the product angular distribution. Finally, the (real) renormalized PDDCSs, $\rho_{q\pm}^{\{k\}}(\theta)$, are obtained from the (complex) $\rho_q^{(k)}(\theta)$ PDDCSs using the Hertel-Stoll normalization.[49]

Calculations were also performed using a QM hard-shell model, in which the potential is infinite within a boundary $\boldsymbol{R}_E$ and zero outside. These QM calculations treat the NO(X) molecule as a closed shell species and were performed using the method of Bosanac and Petrovic.[50,51] The hard-shell potential contours were obtained by intersecting the unmodified $\mathrm{V_{sum}}(R,\gamma)$ potential at 514cm^{-1}.[51] For the mass and collision energy of the system, rotational states up to $j = 23$ and partial waves up to $J = 100$ were included in order to converge the calculations.

III. RESULTS AND DISCUSSION

A. Spin-orbit conserving DCSs

The ion-images for a range ($j' = 4.5 \rightarrow j' = 15.5$) of spin-orbit conserving $f \rightarrow f$ (top panel) and $f \rightarrow e$ (bottom panel) transitions are shown in Fig. 2. The top row in each displays the experimental ion images and the fitted images are shown below. The direction of the initial relative velocity (in this case $\boldsymbol{v}_{\mathrm{rel}} = \boldsymbol{v}_{\mathrm{NO}} - \boldsymbol{v}_{\mathrm{Kr}}$) is indicated by the white arrow, such that intensity in the top left of the image corresponds to forwards scattered NO(X) products and intensity in the bottom right to backwards scattering. The $\mathrm{R_{21}}$ spectroscopic branch or the overlapping $\mathrm{Q_{11}}$ + $\mathrm{P_{21}}$ branches were used to record the $f \rightarrow f$ images, while the $f \rightarrow e$ images were recorded using either the $\mathrm{P_{11}}$ or $\mathrm{R_{11}}$ + $\mathrm{Q_{21}}$ branches. The branch used depended on a several factors, including signal levels for the state and the congestion of the spectrum around the wavelength. The images displayed were all recorded with horizontally polarized light. The corresponding images obtained with vertical polarisation were also recorded and analysed, but are not displayed here.

There are a number of qualitative trends with j' that can be seen in the images. Firstly, the size of the ion image decreases with increasing final rotational level. This is due to a

larger proportion of the collision energy being transferred into rotational energy, resulting in a smaller outgoing translational energy with increasing Δj. It can also be seen that as the rotational state increases the scattering shifts from predominantly forwards scattering (at low j') to sideways and backwards scattering for higher (j'). This observation can be rationalized by considering that collisions that result in little rotational excitation are due to glancing collisions, in which the NO molecule is minimally deflected, whereas head on collisions that result in sideways and backwards scattering are required for large amounts of rotational excitation.

The data were fit using the method outlined in Section II B, and the fitted images are displayed below the corresponding experimental image. The agreement between the experimental and fitted images is good, lending confidence to the parameters chosen for the basis sets. The DCSs derived from the experimental images are displayed for spin-orbit conserving $f \rightarrow f$ and $f \rightarrow e$ transitions in Figs. 3 and 4, respectively. Because the experiment yields only the angular distribution of the scattered products, rather than the differential cross section, the experimental data were separately scaled to the QM results by normalizing the experimental DCSs to the area under the theoretical DCSs. Agreement between the experimental (red line) and theoretical (black line) DCSs is, in general, very good. The very rapid oscillations present in the forward scattered direction of the quantum mechanical calculations cannot be resolved in the experimental data. The velocity distributions in the molecular beams, as well as other factors such as the size of the detection volume, cause these to be blurred out. Recent experiments have used Stark deceleration techniques to select a very narrow velocity distribution of the NO(X) molecular beam,[30] allowing these oscillations to be resolved in the NO(X) + He, Ne and Ar systems.

As noted in Section I, the parity of the NO(X) wavefunction is given by $p = \epsilon(-1)^{j-\frac{1}{2}}$, where $\epsilon = +1$ for the e and $\epsilon = -1$ for the f Λ-doublet levels. A number of parity dependent effects can be seen in the DCSs. Starting from $j = 0.5$ and $\epsilon = -1$, parity conserving (changing) transitions are those for which $\epsilon'(-1)^{\Delta j} = -1(+1)$. The magnitude of the DCS is much larger for parity conserving transitions (such as parity conserving $j' = 5.5, e$ compared to parity changing $j' = 5.5, f$), as a consequence of the near homonuclear nature of the NO(X) molecule. Parity conserving transitions also exhibit multiple peaks in the DCSs, for example $j' = 10.5, f$, which are not observed in the parity changing DCSs, such as $j' = 10.5, e$. As noted in Section I, these effects have been shown to be due to

quantum interference between trajectories scattering from different regions of the molecule for the NO(X) + Ar system,[26,27,35] and have also been observed for NO(X) + Ne.[28] Previous experiments on NO(X) + He did not see such parity dependent oscillations at the collision energy of the experiment,[24,25] although they were predicted for higher collision energies.[52,53]

The similarity of the DCSs for the 'parity pairs' of states with a common value of $n = j' - \epsilon\epsilon'/2$ has already been noted.[24,26–28,35] Compared to NO(X) scattering by He, Ne, and Ar, the parity pair behavior is somewhat less apparent in the case of Kr. For example, the parity pairs connected by $n = 10$ ($j' = 10.5, f$ and $j' = 9.5, e$) and $N = 12$ ($j' = 12.5, f$ and $j' = 11.5, e$) show noticeably different DCSs for NO(X) + Kr, differences which are generally less apparent in the lighter collision systems. The parity pair behavior arises because states with the same n are directly coupled by the same terms in the interaction potential.[52,53] However, as the scattering becomes less direct, and the scattering takes place through tiers of virtual states,[52,53] more terms in the interaction potential are involved in coupling each initial and final state. The similarity of the DCSs within a given parity pair therefore becomes less apparent.

B. Spin-orbit changing DCSs

Experimental and fitted images are shown in the top panels of Figs. 5 and 6 for spin-orbit changing $f \rightarrow f$ and $f \rightarrow e$ transitions. $f \rightarrow f$ transitions were recorded using the R_{22} or $Q_{12} + P_{22}$ branches, and the $f \rightarrow e$ transitions were recorded using the overlapping $Q_{22} + R_{12}$ branches. Similar trends to those observed in spin-orbit conserving transitions can be seen, and the discussion will not be repeated here. The spin-orbit changing images have a signal-to-noise ratio that is slightly worse than for the spin-orbit conserving transitions due to the lower integral cross sections. Again, agreement between the experimental and fitted images is good and the extracted DCSs are compared to the corresponding quantum calculations in the bottom panels. As discussed in Section I, spin-orbit changing collisions can be considered to take place on the $V_{\rm diff}(R, \gamma)$ potential. This is calculated using Eq. (2), so is much more sensitive to inaccuracies in the $V_{A'}$ and $V_{A''}$ surfaces than the $V_{\rm sum}(R, \gamma)$ surface. As such, the good agreement between experiment and theory for the spin-orbit changing transitions confirms the high degree of accuracy of the potential energy surface for these calculations.

Overall, the DCSs for the spin-orbit changing transitions show similar parity pair behavior as the spin-orbit conserving transitions.

C. Collision induced alignment

The experimental images for collision-induced alignment are shown in Fig. 7 for a range of spin-orbit conserving $f \rightarrow f$ states. The collision-induced alignment images are obtained by recording individual DCS images with horizontally and vertically polarized light and taking the normalized difference, $(I_{\mathrm{V}} - I_{\mathrm{H}})/(I_{\mathrm{V}} + I_{\mathrm{H}})$, of the images. This minimizes the effect of the DCS weighting and flux density correction on the alignment information.[12,29] The overall agreement between the experimental, simulated and fitted images is very good, with the depolarisation correction often accounting for the asymmetry in the images. In areas of the image where the DCS is small, for example at scattering angle greater than 80° for $j' = 7.5$, the experimental intensity is low and so no alignment information can be obtained.

In these normalized difference images, areas of black indicate no alignment of $\boldsymbol{j'}$, red or green indicates $I_{\mathrm{V}} > I_{\mathrm{H}}$ and blue or purple corresponds to $I_{\mathrm{H}} > I_{\mathrm{V}}$. Low and medium rotational states ($j' \leq 12.5$) were recorded using the R_{21} spectroscopic branch. For an R branch transition the transition dipole moment, $\boldsymbol{\mu}$, is perpendicular to the molecular axis, $\boldsymbol{r}$ and $\boldsymbol{j'}$ in the high j limit. Since the probability of absorbing a photon is maximum when the electric vector of the light, $\boldsymbol{\epsilon}$, is parallel to $\boldsymbol{\mu}$, and a minimum when the two vectors are perpendicular, it follows that when $I_{\mathrm{V}} > I_{\mathrm{H}}$, $\boldsymbol{j'}$ will lie in the plane defined by the molecular beams, corresponding to 'propeller' like rotation. Likewise when $I_{\mathrm{H}} > I_{\mathrm{V}}$, $\boldsymbol{j'}$ will lie out of the molecular beam plane, so the molecule is rotating like a 'frisbee'. For all states recorded using R branch excitation, the positive intensity that can be seen in the forward scattered direction corresponds to propeller like rotation. As the scattering angle increases, the intensity becomes less positive and then negative indicating the transition to 'frisbee' like rotation in the very backward scattered direction. The extent of the 'propeller' like rotation decreases with increasing rotational excitation.

For high rotational states ($j' \geq 13.5$) the overlapping Q_{11}+P_{21} branch was used, due to the small cross sections. In the case of Q branch transitions, $\boldsymbol{\mu}$ lies parallel to $\boldsymbol{j'}$ and perpendicular to the molecular axis, therefore $I_{\mathrm{V}} > I_{\mathrm{H}}$ will correspond to the molecule

rotating like a 'frisbee' and when $I_H > I_V$ the rotation of the molecule will resemble that of a propeller. For P branch transitions, $\boldsymbol{\mu}$ is, as in the case of R branch transitions, perpendicular to $\boldsymbol{j'}$. Since the intensity of the Q branch is approximately twice as sensitive to alignment than the P branch, the contribution from the Q branch will dominate. Note that the intensity of the images is inverted compared with the experimental images recorded with only R branch excitation. The extent of 'propeller' like rotation is very small for $j' = 13.5$, and for the highest j' states, only 'frisbee' like rotation is observed.

The above observations can be explained qualitatively by considering the classical kinematic apse model,[54] which has previously been used to explain collision-induced alignment for collisions of NO(X) + Ar.[12,29] The kinematic apse lies in the scattering plane and is defined as:

$$\hat{\boldsymbol{a}} = \frac{\boldsymbol{k'} - \boldsymbol{k}}{|\boldsymbol{k'} - \boldsymbol{k}|}\,, \tag{11}$$

where $\boldsymbol{k}$ and $\boldsymbol{k'}$ are the initial and final relative velocities. For a classical collision between hard-shell particles, the projection quantum number of $\boldsymbol{j'}$ onto the apse, m_a, is conserved before and after collision. Since the NO(X) is prepared in its lowest rotational state, $j = 0.5$, the projection onto the apse will be $m_a = \pm 0.5$, and therefore the rotational angular momentum after the collision must be near-perpendicular to the apse direction. Fig. 8 shows experimental and apse model simulations for $j' = 6.5$ and $j' = 15.5$. The apse model predicts the 'propeller' like rotation for forward scattering at low rotational excitation, and 'frisbee' like rotation in the backwards scattered direction and at high j'. To rationalize this observation it is helpful to consider where the apse lies in each case, as shown schematically the right panel of Fig. 8. For forward scattering at low j' (panel a), $\boldsymbol{a}$ lies almost perpendicular to $\boldsymbol{k}$, which after averaging over the azimuthal angle ($\boldsymbol{k'}$ can point to anywhere on the green dotted circle) results in a polarisation of $\boldsymbol{j'}$ in the plane defined by the molecular beams, corresponding to the radical rotating like a propeller. In the backward scattered direction (panel b) the apse has a greater component parallel to $\boldsymbol{k}$, resulting in a polarisation of $\boldsymbol{j'}$ more perpendicular to the molecular beam plane, corresponding to frisbee like rotation of the molecule. As rotational excitation increases, the extent of propeller like rotation decreases until at high j', only frisbee like rotation is observed. Due to the increased rotational excitation of the molecule, the outgoing velocity, $\boldsymbol{k'}$ decrease, resulting in a smaller Newton sphere as shown in panel c. In this case, $\boldsymbol{a}$ now has a significant component parallel to $\boldsymbol{k}$, resulting in frisbee like rotation even at small scattering angles.

Qualitative inspection of the normalized difference images in Figs. 7 and 8 suggests that even for the relatively attractive NO(X) + Kr system, the propensity to conserve the projection of $\boldsymbol{j'}$ along the kinematic apse is dominant feature of the rotation alignment data.

The renormalized PDDCSs derived from fits to the experimental images are shown in Figs. 9 and 10 for spin-orbit conserving $f \rightarrow f$ transitions, where they are compared with CC QM calculations. The experimental and CC QM DCSs are also shown in the left hand column. Agreement between the experimental and theoretical PDDCSs is very good across the entire range of transitions.

The $\rho_0^{\{2\}}(\theta)$ moment quantifies the alignment of $\boldsymbol{j'}$ with respect to $\boldsymbol{k}$, with positive values indicating $\boldsymbol{j'}$ is parallel to $\boldsymbol{k}$, and negative values indicating alignment of $\boldsymbol{j'}$ perpendicular to the scattering plane.[29,55] Features such as the change in sign of the $\rho_0^{\{2\}}(\theta)$ at small scattering angles for $j' = 5.5$ is captured in the experimental data, however, some sharper features, such as the oscillation in the $\rho_0^{\{2\}}(\theta)$ at approximately 70° in $j' = 6.5$ cannot be resolved due to the number of moments used in the fit. At high j' ($j' > 14.5$), the experimental $\rho_0^{\{2\}}(\theta)$ seems to indicate stronger alignment than the QM calculations predict. These transitions were recorded using a mixed Q and P branch, so the sensitivity of the intensity on alignment will vary slightly depending on the part of the line used to probe the transition. For this reason it is preferable to use non-overlapping branches where possible.

In the QM data, as the scattering angle goes to 0°, the $\rho_0^{\{2\}}(\theta)$ moments tends to its limiting value of around -0.5, and the $\rho_{2+}^{\{2\}}(\theta)$ to 0, corresponding to $\boldsymbol{j'}$ lying perpendicular to the molecular beam plane or frisbee like rotation.[56] At 0°, $\boldsymbol{k'}$ lies completely parallel to $\boldsymbol{k}$, so the apse will be antiparallel to $\boldsymbol{k}$ and $\boldsymbol{j'}$ will be required to be perpendicular to the plane defined by the molecular beams, so $\rho_0^{\{2\}}(\theta)$ will tend to its limiting value. Oscillations in the QM data can be seen at the same scattering angle in both PDDCSs and the DCS, for example at approximately 95° in the $j' = 8.5$ transition. The oscillations in the DCS have previously been shown to be due to interference from trajectories sampling different regions of the potential. A weak parity dependence is seen in these oscillations, with the features being more prominent in transitions in which the total parity of the NO wavefunction is conserved throughout the collision.

The $\rho_{2+}^{\{2\}}(\theta)$ moment describes the preference for alignment of $\boldsymbol{j'}$ about the scattering frame x or y axes.[29,55] The $\rho_{2+}^{\{2\}}(\theta)$ moment is generally found to be negative, consistent with alignment of $\boldsymbol{j'}$ out of the scattering frame, along the scattering frame y-axis. Similar

behavior has been found to NO(X) + Ar.[29] In previous work on NO(X) + Ar, it was found that the $\rho_{2+}^{\{2\}}(\theta)$ was systematically slightly underestimated.[28] This was attributed to the distorting effect of the slight asymmetry in the images. In the present work, there seems to be no such systematic underestimation of the $\rho_{2+}^{\{2\}}(\theta)$, as the asymmetry in the image has been accounted for during the fitting procedure as described in Section II B.

Experimental alignment images for spin-orbit changing collisions $j' = 5.5, e$ and $j' = 9.5, e$ are shown in Fig. 11 along with QM simulations, fits and V+H DCS images. Both images were recorded using the Q_{22}+R_{12} overlapping spectroscopic branch. As discussed previously, areas of negative intensity indicate propeller like rotation of the radical and positive intensity corresponds to frisbee like rotation. The extent of propeller like rotation in $j' = 9.5$ is much less than for the corresponding spin-orbit conserving transition, due to the smaller value of $\boldsymbol{k}'$ (the upper spin-orbit level lies approximately $123\,\mathrm{cm}^{-1}$ above the lower), resulting in a greater alignment of the kinematic apse parallel to $\boldsymbol{k}$ similar to the case with high j' shown in Fig. 8. It should also be noted that the DCSs for the spin-orbit changing collisions show significantly more sideways and backward scattering than the corresponding spin-orbit conserving transitions. This reflects the fact that partial waves with lower J (or lower impact parameters) contribute to the DCSs for spin-orbit changing collisions compared with the spin-orbit conserving transitions.[52,53] The experimental DCSs and $\rho_0^{\{2\}}(\theta)$ and $\rho_{2+}^{\{2\}}(\theta)$ moments are compared to the CC QM calculations in the bottom panel of Fig. 11. Agreement between experiment and theory again is very good. Undulations in the three sets of data can be seen at the same scattering angle (approximately 70° for $j' = 9.5$), however, they appear much less prominent than in the spin-orbit conserving data.

D. Comparison with NO(X) + argon and with model calculations

As discussed previously, collision-induced alignment in the NO(X) + Ar system has been extensively studied.[9,12,29,36,37] Switching the colliding partner from Ar to Kr results in a number of changes to the system. Firstly, the NO(X) + Kr potential energy surface is more attractive than that for NO(X) + Ar, with well depths of $147\,\mathrm{cm}^{-1}$ (A' surface) and $143\,\mathrm{cm}^{-1}$ (A'' surface)[4] compared to well depths of $116\,\mathrm{cm}^{-1}$ (A' surface) and $111\,\mathrm{cm}^{-1}$ (A'' surface) in the case of NO(X) + Ar.[3] Furthermore, there are also subtle differences in the range and anisotropy of the potentials for the two systems, most notable in the attractive regions of

the surfaces.[3,4] It should also be noted that, whilst the experimental collision energy of the system remains largely unchanged (530 cm^{-1} for NO(X) + Ar and 514 cm^{-1} for NO(X) + Kr), the increase in reduced mass results in a ∼12% smaller de Broglie wavelength in the NO(X) + Kr system. In this Section we will explore the similarity and differences between the two systems, and the effect these have on the ability of the apse model to correctly account for the collision-induced alignment.

Fig. 12 shows a comparison of CC QM (black continuous line) and QM hard-shell (red dashed line) DCSs for both the NO(X) + Ar (left) and NO(X) + Kr (right) systems. The open shell CC QM data obtained using the full potential are for the $f \rightarrow f$ transitions, which are parity conserving for even Δj and parity changing for odd Δj. The QM data obtained using the hard-shell potential involve the same parity changing collisions as the open shell $f \rightarrow f$ transitions, but note that these calculations treat NO as a closed shell species.[51] The CC QM DCSs for NO(X) + Ar and NO(X) + Kr share many similar features, such as the overall magnitudes and position and number of peaks. The main difference can be seen in the forward scattered region, where the DCS for NO(X) + Kr is larger than that for the corresponding NO(X) + Ar transition. Trajectories that sample the attractive region of the potential are more likely to be forward scattered, so an enhancement in the DCS in the forwards scattered region is seen for the more attractive NO(X) + Kr system.

The QM hard-shell calculations remove the effect of the attractive part of the potential, and also the finite range of the repulsive wall. The QM hard-shell data correctly predicts the number of peaks in the DCSs. However, the peaks are shifted to larger scattering angles than in the CC QM calculations due to the absence of attractive forces, and the model QM calculations also over-estimate the integral cross sections for the high Δj transitions. The QM hard-shell model predicts two prominent peaks for NO(X) + Ar $j' = 10.5$, but three prominent peaks for NO(X) + Kr. As noted above, these oscillations have previously been shown to be dependent on interference from trajectories sampling different regions of the potential, and the frequency of the oscillations is dependent on the de Broglie wavelength ($\lambda = h/p$) of the system, and on the range and anisotropy of the interaction between NO(X) and the rare gas.[26,27,35] In particular, for parity conserving transitions, such as the ones shown, at fixed de Broglie wavelength, the frequency of the oscillations depends to a good approximation on the difference in the major and minor rigid ellipse parameters, $(A_N - B)$ and $(A_O - B)$.[26,27,35] Although the range of the PES sampled at the collision of

the experiment is somewhat larger for Kr than for Ar, the potential for Kr is slightly more spherical, and this effect alone would result in fewer oscillations being observed in the DCSs in the case of Kr. Counteracting the effect of the anisotropy in the PES, the decrease in the de Broglie wavelength of the NO(X) + Kr collision pair compared with NO(X) + Ar leads to an increase in the number of oscillations. Thus, overall, the change in the de Broglie wavelength is the dominant effect responsible for the increase in the number of oscillations in the Kr system relative to scattering with Ar.

CC QM and QM hard-shell $\rho_0^{\{2\}}(\theta)$ alignment moments are shown in the second and fourth columns of Fig. 12, along with the results of the kinematic apse model. The agreement between the $\rho_0^{\{2\}}(\theta)$ alignment moments determined from all three calculations is generally quite good. Apart from the lowest rotation state shown ($j' = 5.5, f$, see below), the CC QM and QM hard-shell $\rho_0^{\{2\}}(\theta)$ moments are in excellent agreement for both the Ar and Kr collision systems. Slight undulations can be seen in both the QM hard-shell and CC QM calculations at sideways scattering angles, such as at approximately 100° for $j' = 8.5$ in the CC QM calculations. The undulations in the CC QM data are not reproduced quantitatively by the QM hard-shell, and, unsurprisingly, are not observed at all in the apse model calculations. At low j', very rapid oscillations are found in the extreme forward scattered region of the QM hard-shell and CC QM calculations, both in the DCSs and the alignment moments, which again are not observed in the apse model calculations. These rapid oscillations can be described well by the Fraunhofer diffraction model.[57,58] Such quantum mechanical interference structure is not allowed for in the classical kinematic apse model, but are seen in the QM hard-shell calculations.

The kinematic apse model describes a purely classical impulsive collision, taking place at a specific point on the surface of the hard-shell, so it may be expected that the QM hard-shell calculations, in which the interaction potential is purely repulsive, and the apse model should agree very well. The agreement between the QM hard-shell and apse model $\rho_0^{\{2\}}(\theta)$ alignment moments is good, particularly for large scattering angles, although deviations are seen in the forwards scattered region. This disagreement increases with increasing j', in spite of the fact that collisions that result in large amounts of rotational excitation might be expected to be more impulsive.

To understand the disagreement between the classical apse model and the QM hard-shell calculations, one has to consider the QM encounter in more detail. The condition of the apse

model, that the projection of j on the apse is conserved throughout the course of collision, will be true only in the energy sudden limit,[54] in which the molecule rotates slowly enough to be considered nearly stationary during the interaction time. For low final rotational states, the NO(X) molecule will be rotating slowly, and the atom will depart almost as quickly from the encounter region as it did on approach. As more rotational energy is transferred to the molecule, the NO(X) will be rotating faster and less kinetic energy will be available to the atom. This results in an increase in the interaction time, and so the quantum mechanical encounter will sample a larger range of bond axis orientations, and the collision can no longer be assumed to have occurred at a specific point on the molecule.[51] In the case of a forward scattered collision, the atom will stay close to the molecule for a longer time period than in a backward scattered collision, because the former collisions are dominated by large impact parameters, which cause the radial kinetic energy to be small. The projection of j onto the kinematic apse in the QM encounter is less well conserved for such collisions, and the deviations from the apse model are thus more pronounced for low scattering angles and at high j'.[59]

For NO(X) + Kr collisions leading to $j' = 5.5, f$ it can be seen that the apse model and QM hard-shell calculations both agree in predicting positive $\rho_0^{\{2\}}(\theta)$ values between 0 and 45°, whereas the full CC QM calculations show a change in sign. This feature is a signature of the attractive forces in the system.[60] The change of sign in the CC QM $\rho_0^{\{2\}}(\theta)$ data is not present in the calculations for the NO(X) + Ar system, reflecting the more constrained range of attractive forces in the Ar case. Recent work on the NO(A) + Ne system,[61] which has considerably weaker attractive forces than NO(X) + Ar or Kr, attributed deviations between quantum mechanical and apse model PDDCSs to the finite range of the repulsive potential. Although the range of repulsive potential might play some role for NO(X) + Kr, it does not appear to be the dominant mechanism for the breakdown in the apse model in this system. The hard-shell QM calculations, in which the finite range of the potential is removed, show good agreement with the full CC QM calculations for moderate to high Δj transitions, for which the repulsive part of the potential is mainly sampled. In the present case, deviations between the apse, hard-shell QM, and full CC QM calculations are more noticeable at low Δj, in the forward scattered region, which is more dominated by the attractive part of the potential, precisely where one might expect the apse and QM hard-shell models to fail.

IV. SUMMARY

Inelastic collisions of fully Λ-doublet quantum state selected and resolved NO(X) with krypton have been investigated. Experimental DCSs for both spin-orbit conserving and changing collisions have been compared with CC QM calculations and have been found to be in good agreement. Collision-induced alignment has also been studied, and the $\rho_0^{\{2\}}(\theta)$ and $\rho_{2+}^{\{2\}}(\theta)$ alignment moments have been compared with theoretical calculations for a range of spin-orbit and parity conserving and changing states. The alignment moments were shown to be in good agreement with the CC QM calculations across all transitions. A comparison with the NO(X) + Ar system revealed that the attractive nature of the NO(X) + Kr PES results in an enhancement in the forward scattered region of the DCS. Comparison of the alignment moments highlighted differences at low j', where the kinematic apse results and QM hard-shell calculations are less reliable for NO(X) + Kr. However, for higher j', despite the difference in the two systems, the apse model predicts the rotational alignment in both systems almost as equally well, with discrepancies between the classical apse model and CC QM calculations likely due to the finite interaction region of the QM encounter.

ACKNOWLEDGMENTS

The support of the UK EPSRC (to M.B. *via* Programme Grants EP/G00224X/1 and EP/L005913/1), the EU (to M.B. *via* FP7 EU People ITN project 238671), and the Spanish Ministry of Science and Innovation and of Economy and Competitiveness (grants CTQ2008-02578, CTQ2012-37404, and CSD200900038) are gratefully acknowledged. S.S. acknowledges support from the National Basic Research Program of China (973 program) under grant No. 2013CB922200 and from the National Science Foundation of China under grant Nos. 11034003 and 91221301.

REFERENCES

[1]M. H. Alexander, J. Chem. Phys. **76**, 5974 (1982).

[2]M. H. Alexander, Chem. Phys. **92**, 337 (1985).

[3]M. H. Alexander, J. Chem. Phys. **111**, 7426, (1999).

[4]B. Wen, H. Meyer, J. Kłos, and M. H. Alexander, J. Phys. Chem. A **113**, 7366 (2009).

[5]M. H. Alexander, P. Soldan, T. G. Wright, Y. Kim, H. Meyer, P. J. Dagdigian, and E. P. F. Lee, J. Chem. Phys. **114**, 5588 (2001).

[6]J. Kłos, G. Chalasinski, M. T. Berry, R. Bukowski, and S. M. Cybulski, J. Chem. Phys. **112**, 2195 (2000).

[7]J. Kłos, F. J. Aoiz, M. Menendez, M. Brouard, H. Chadwick, and C. J. Eyles, J. Chem. Phys. **137**, 014312 (2012).

[8]P. Casavecchia, A. Laganá, and G. G. Volpi, Chem. Phys. Lett. **112**, 445 (1984).

[9]J. I. Cline, K. T. Lorenz, E. A. Wade, J. W. Barr, and D. W. Chandler, J. Chem. Phys. **115**, 6277 (2001).

[10]K. T. Lorenz, D. W. Chandler, J. W. Barr, W. Chen, G. L. Barnes, and J. I. Cline, Science **293**, 2063 (2001).

[11]M. S. Elioff and D. W. Chandler, J. Chem. Phys. **117**, 6455 (2002).

[12]E. A. Wade, K. T. Lorenz, D. W. Chandler, J. W. Barr, G. L. Barnes, and J. I. Cline, Chem. Phys. **301**, 261 (2004).

[13]M. J. L. de Lange, M. M. J. E. Drabbels, P. T. Griffiths, J. Bulthuis, S. Stolte, and J. Snijders, Chem. Phys. Lett. **313**, 491 (1999).

[14]A. A. Dixit, P. J. Pisano, and P. L. Houston, J. Phys. Chem. **105**, 11165 (2001).

[15]S. D. Jons, J. E. Shirley, M. T. Vonk, C. F. Giese, and W. R. Gentry, J. Chem. Phys. **105**, 5397 (1996).

[16]S. D. Jons, J. E. Shirley, M. T. Vonk, C. F. Giese, and W. R. Gentry, J. Chem. Phys. **97**, 7831 (1992).

[17]A. G. Suits, L. S. Bontuyan, P. L. Houston, and B. J. Whitaker, J. Chem. Phys. **96**, 8618 (1992).

[18]L. S. Bontuyan, A. G. Suits, P. L. Houston, and B. J. Whitaker, J. Phys. Chem. **97**, 6342 (1993).

[19]A. Lin, S. Antonova, A. P. Tsakotellis, and G. C. McBane, J. Phys. Chem. **103**, 1198 (1999).

[20]J. J. Van Leuken, F. H. W. Van Amerom, J. Bulthuis, J. G. Snijders, and S. Stolte, J. Phys. Chem. **99**, 15573 (1995).

[21]H. Meyer, J. Chem. Phys. **102**, 3151 (1995).

[22]Y. Kim, H. Meyer, and M. H. Alexander, J. Chem. Phys. **121**, 1339 (2004).

[23]Y. Kim and H. Meyer, Chem. Phys. **301**, 273 (2004).

[24]A. Gijsbertsen, H. Linnartz, G. Rus, A. E. Wiskerke, S. Stolte, D. W. Chandler, and J. Kłos, J Chem. Phys. **123**, 224305 (2005).

[25]A. Gijsbertsen, H. Linnartz, and S. Stolte, J. Chem. Phys. **125**, 133112 (2006).

[26]C. J. Eyles, M. Brouard, C. H. Yang, J. Kłos, F. J. Aoiz, A. Gijsbertsen, A. E. Wiskerke, and S. Stolte, Nat. Chem. **3**, 597 (2011).

[27]C. J. Eyles, M. Brouard, H. Chadwick, B. Hornung, B. Nichols, C. H. Yang, J. Kłos, F. J. Aoiz, A. Gijsbertsen, A. E. Wiskerke, and S. Stolte, Phys. Chem. Chem. Phys. **14**, 5403 (2012).

[28]M. Brouard, H. Chadwick, C. J. Eyles, B. Hornung, B. Nichols, J. M. Scott, F. J. Aoiz, J. Kos, S. Stolte, and X. Zhang, Mol. Phys. **111**, 1759 (2013).

[29]M. Brouard, H. Chadwick, C. J. Eyles, B. Hornung, B. Nichols, F. J. Aoiz, P. G. Jambrina, and S. Stolte, J. Chem. Phys. **138**, 104310 (2013).

[30]A. von Zastrow, J. Onvlee, S. N. Vogels, G. C. Groenenboom, A. van der Avoird, and S. Y. T. van de Meerakker, Nat. Chem. **6**, 216 (2014).

[31]T. Orlikowski and M. H. Alexander, J. Chem. Phys. **79**, 6006 (1983).

[32]M. H. Alexander and T. Orlikowski, J. Chem. Phys. **80**, 1506 (1984).

[33]G. C. Corey and M. H. Alexander, J. Chem. Phys. **85**, 5652 (1986).

[34]F. J. Aoiz, J. E. Verdasco, V. J. Herrero, V. S. Rabanos, and M. H. Alexander, J. Chem. Phys. **119**, 5860 (2003).

[35]C. J. Eyles, M. Brouard, H. Chadwick, F. J. Aoiz, J. Kłos, A. Gijsbertsen, X. Zhang, and S. Stolte, Phys. Chem. Chem. Phys. **14**, 5420 (2012).

[36]M. Brouard, H. Chadwick, C. J. Eyles, B. Hornung, B. Nichols, F. J. Aoiz, P. G. Jambrina, S. Stolte, and M. P. de Miranda, J. Chem. Phys. **138**, 104309 (2013).

[37]M. H. Alexander, Fara. Disc. **113**, 437 (1999).

[38]S. Marinakis, B. J. Howard, F. J. Aoiz, and J. Kłos, Chem. Phys. Lett. **512**, 161 (2011).

[39]A. T. J. B. Eppink and D. H. Parker, Rev. Sci. Instrum. **68**, 3477 (1997).

[40]D. W. Chandler and P. L. Houston, J. Chem. Phys. **87**, 1445 (1987).

[41]G. Paterson, A. Relf, M. L. Costen, K. G. McKendrick, M. H. Alexander, and P. J. Dagdigian, J. Chem. Phys. **135**, 234304 (2011).

[42]G. Paterson, M. L. Costen, and K. G. McKendrick, Int. Rev. Phys. Chem. **31**, 69 (2012).

[43]H. Chadwick, M. Brouard, T. Perkins, and F. J. Aoiz, Int. Rev. Phys. Chem. **33**, 79 (2014).

[44]M. J. Bass, M. Brouard, A. P. Clark, and C. Vallance, J. Chem. Phys. **117**, 8723 (2002).

[45]HIBRIDON is a package of programs for the time-independent quantum treatment of inelastic collisions and photodissociation written by M. H. Alexander, D. E. Manolopoulos, H.-J. Werner, and B. Follmeg, with contributions by P. F. Vohralik, D. Lemoine, G. Corey, R. Gordon, B. Johnson, T. Orlikowski, A. Berning, A. Degli-Esposti, C. Rist, P. Dagdigian, B. Pouilly, G. van der Sanden, M. Yang, F. de Weerd, S. Gregurick, and J. Kłos.

[46]M. H. Alexander and D. E. Manolopoulos, J. Chem. Phys. **86**, 2044 (1987).

[47]Y. Kim, J. Fleniken, H. Meyer, M. H. Alexander, and P. J. Dagdigian, J. Chem. Phys. **113**, 73 (2000).

[48]P. G. Jambrina, J. Aldegunde, M. P. de Miranda, V. Sáez-Rábanos, and F. J. Aoiz, Phys. Chem. Chem. Phys. **14**, 9977 (2012).

[49]J. Aldegunde, J. M. Haigh, M. P. de Miranda, B. K. Kendrick, V. Sáez-Rábanos, and F. J. Aoiz, J. Phys. Chem. A **109**, 6200 (2005).

[50]S. D. Bosanac and N. Petrovic, Phys. Rev. A **41** (1990).

[51]M. Brouard, B. Hornung, and F. J. Aoiz, Phys. Rev. Lett. **111** (2013).

[52]J. Kłos, F. J. Aoiz, J. E. Verdasco, M. Brouard, S. Marinakis, and S. Stolte, J. Chem. Phys. **127**, 031102 (2007).

[53]F. J. Aoiz, J. E. Verdasco, M. Brouard, J. Kłos, S. Marinakis, and S. Stolte, J. Phys. Chem. A **113**, 14636 (2009).

[54]V. Khare, D. J. Kouri, and D. K. Hoffman, J. Chem. Phys. **74**, 2275 (1981).

[55]M. P. de Miranda, F. J. Aoiz, L. Bañares, and V. S. Rábanos, J. Chem Phys. **111**, 5368 (1999).

[56]F. J. Aoiz, M. Brouard, and P. A. Enriquez, J. Chem. Phys. **105**, 4964 (1996).

[57]M. Faubel, J. Chem. Phys. **81**, 5559 (1984).

[58]M. Lemeshko, P. G. Jambrina, M. P. de Miranda, and B. Friedrich, J. Chem. Phys. **132**, 161102 (2010).

[59]B. Hornung, *Rotational polarization effects in the inelastic scattering of NO(X) with Ar* (D.Phil. Thesis, Oxford University, Oxford, U.K., 2013).

[60]H. Chadwick, B. Nichols, S. D. S. Gordon, B. Hornung, M. Brouard, J. Kłos, M. H. Alexander, F. J. Aoiz, and S. Stolte, J. Phys. Chem. Lett. **5**, 3296 (2014).

[61]J. D. Steill, J. J. Kay, G. Paterson, T. R. Sharples, J. Kłos, M. L. Costen, K. E. Strecker, K. G. McKendrick, M. H. Alexander, and D. W. Chandler, J. Phys. Chem. A **117**, 8163

(2013).

FIG. 1. Experimental $(I_V - I_H)/(I_V + I_H)$ ion images for spin-orbit conserving transitions to $j' = 6.5, f$ and $j' = 13.5, f$ superimposed with the appropriate Newton triangle for the collision. A schematic of the Newton triangle for the collision is shown in the right hand panel. $\boldsymbol{v}_{NO}$ and $\boldsymbol{v}_{Kr}$ are the lab frame velocities of the NO and Kr molecular beams respectively, and the relativee velocity is defined here as $\boldsymbol{v}_{rel} = \boldsymbol{v}_{NO} - \boldsymbol{v}_{Kr}$. The dashed circles show the Newton spheres for $j' = 6.5$ (green) and $j' = 13.5$ (purple) and $\boldsymbol{v}_{slow}$ indicates the lab frame velocities of the slowest moving molecules for each state.

FIG. 2. Experimental (top row) and fitted (bottom row) ion images for transitions between $|\Omega{=}0.5,\ j{=}0.5,\ f\rangle \rightarrow |\Omega'{=}0.5,\ j',\ f/e\rangle$, as indicated. The initial direction of the centre-of-mass frame velocity of the NO(X) is shown as a white arrow in the top left image. The data were obtained with horizontally polarized probe laser radiation.

FIG. 3. Experimentally determined DCSs (red lines) and QM DCSs (black lines) for the transitions between $|\Omega{=}0.5,\ j{=}0.5,\ f\rangle \rightarrow |\Omega'{=}0.5,\ j',\ f\rangle$. The error bars associated with the experimental data represent 95 % confidence limits. Transitions for which $j' - 0.5$ is even are parity conserving.

FIG. 4. Experimentally determined DCSs (red lines) and QM DCSs (black lines) for the transitions between $|\Omega{=}0.5,\ j{=}0.5,\ f\rangle \rightarrow |\Omega'{=}0.5,\ j',\ e\rangle$. The error bars associated with the experimental data represent 95 % confidence limits. In this case, transitions for which $j' - 0.5$ is odd are parity conserving.

FIG. 5. Top panel: Experimental (top row) and fitted (bottom row) ion images for transitions between $|\Omega{=}0.5,\ j{=}0.5,\ f\rangle \rightarrow |\Omega'{=}1.5,\ j',\ f\rangle$. Bottom panel: Experimentally determined DCSs (red lines) and QM DCSs (black lines) for the transitions shown above. The error bars associated with the experimental data represent 95 % confidence limits.

FIG. 6. Top panel: Experimental (top row) and fitted (bottom row) ion images for transitions between $|\Omega{=}0.5,\ j{=}0.5,\ f\rangle \rightarrow |\Omega'{=}1.5,\ j',\ e\rangle$. Bottom panel: Experimentally determined DCSs (red lines) and QM DCSs (black lines) for the transitions shown above. The error bars associated with the experimental data represent 95 % confidence limits.

FIG. 7. Experimental (left column), simulated (second column) and fitted (third column) normalized difference imagines, $(I_{\rm V} - I_{\rm H})/(I_{\rm V} + I_{\rm H})$, for transitions between $|\Omega{=}0.5,\ j{=}0.5,\ f\rangle \rightarrow |\Omega'{=}0.5,\ j',\ f\rangle$. The experimental $(I_{\rm V} + I_{\rm H})$ images are shown in the right column.

FIG. 8. Comparison of experimental $(I_{\rm V} - I_{\rm H})/(I_{\rm V} + I_{\rm H})$ ion images (left column) and simulations using the apse model, *i.e.* assuming that $\boldsymbol{j'}$ is almost perpendicular to the kinematic apse (middle column), for transitions between $|\Omega{=}0.5,\ j{=}0.5,\ f\rangle \rightarrow |\Omega'{=}0.5,\ j' = 6.5, 15.5,\ f\rangle$. The right hand panel shows schematically the direction of $\boldsymbol{a}$ and $\boldsymbol{j'}$ for a) forward scattering at low j', b) backward scattering at low j' and c) scattering at high j'.

FIG. 9. Comparison of the experimental (red line) and QM (black line) $\rho_0^{\{2\}}(\theta)$ (middle column) and $\rho_{2+}^{\{2\}}(\theta)$ (right column) renormalized PDDCSs for transitions between $|\Omega{=}0.5,\ j{=}0.5,\ f\rangle \rightarrow |\Omega'{=}0.5,\ j',\ f\rangle$, for states from $j' = 5.5, f$ up to $j' = 10.5, f$. The left column shows the experimentally determined DCS (red line) and QM DCS (black line). The error bars associated with the experimental data represent 95 % confidence limits.

FIG. 10. As for Fig. 9, but showing data for final states from $j' = 11.5, f$ to $j' = 16.5, f$.

FIG. 11. Top panel: Experimental (left column), simulated (second column) and fitted (third column) $(I_{\rm V} - I_{\rm H})/(I_{\rm V} + I_{\rm H})$ images for transitions between $|\Omega{=}0.5,\ j{=}0.5,\ f\rangle \rightarrow |\Omega'{=}1.5,\ j',\ e\rangle$. The experimental $(I_{\rm V} + I_{\rm H})$ images are shown in the right column. Bottom panel: Comparison of the experimental (red line) and QM (black line) $\rho_0^{\{2\}}(\theta)$ (middle column) and $\rho_{2+}^{\{2\}}(\theta)$ (right column) renormalized PDDCSs for the transitions shown above. The left column shows the experimentally determined DCS (red line) and QM DCS (black line). The error bars associated with the experimental data represent 95 % confidence limits.

FIG. 12. DCSs and $\rho_0^{\{2\}}(\theta)$ renormalized PDDCSs for the NO(X) + Ar (left) and NO(X) + Kr (right) systems. The collision energies for Ar and Kr systems are $530\,\mathrm{cm}^{-1}$ and $514\,\mathrm{cm}^{-1}$, respectively. CC QM calculations (black continuous lines) are compared with calculations using the QM hard-shell (red dashed line). The apse model $\rho_0^{\{2\}}(\theta)$ renormalized PDDCSs are also shown as blue dotted lines. The open shell CC QM data are for the $f \rightarrow f$ spin-orbit conserving transitions.

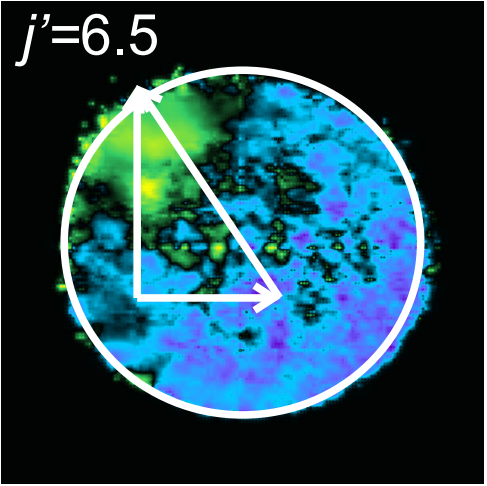
j'=6.5

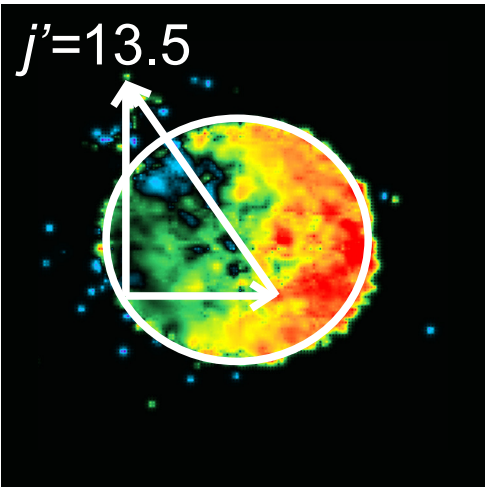
j'=13.5

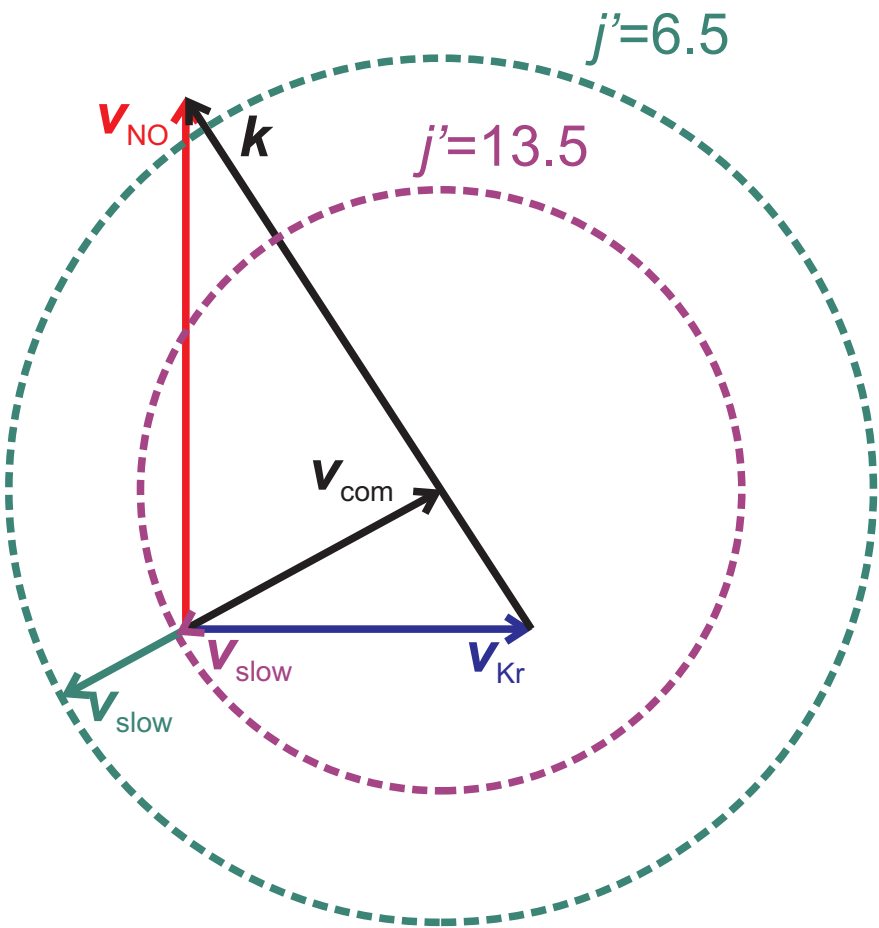
j'=6.5
j'=13.5
v NO
k
v com
v slow
v Kr
v slow

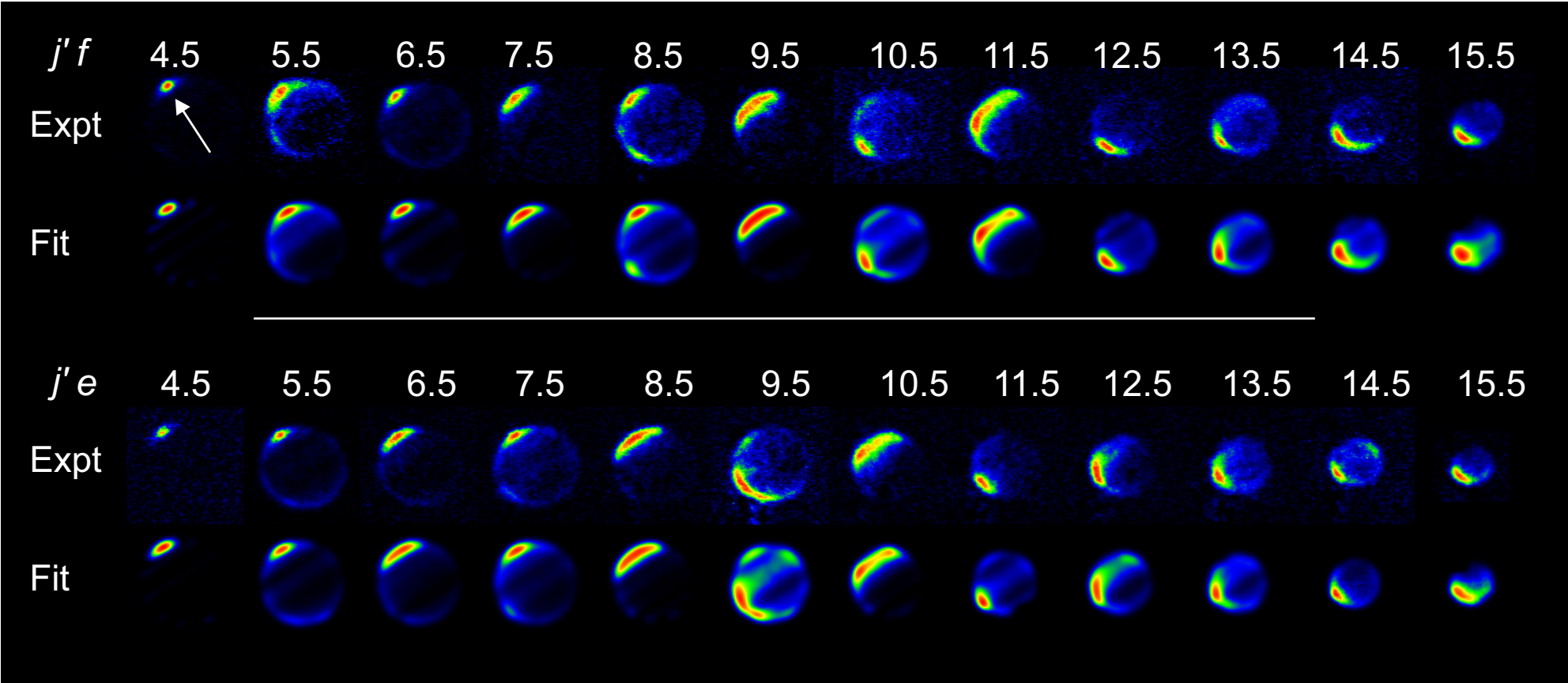
j′ f
4.5
5.5
6.5
7.5
8.5
9.5
10.5
11.5
12.5
13.5
14.5
15.5
Expt
Fit
j′ e
4.5
5.5
6.5
7.5
8.5
9.5
10.5
11.5
12.5
13.5
14.5
15.5
Expt
Fit

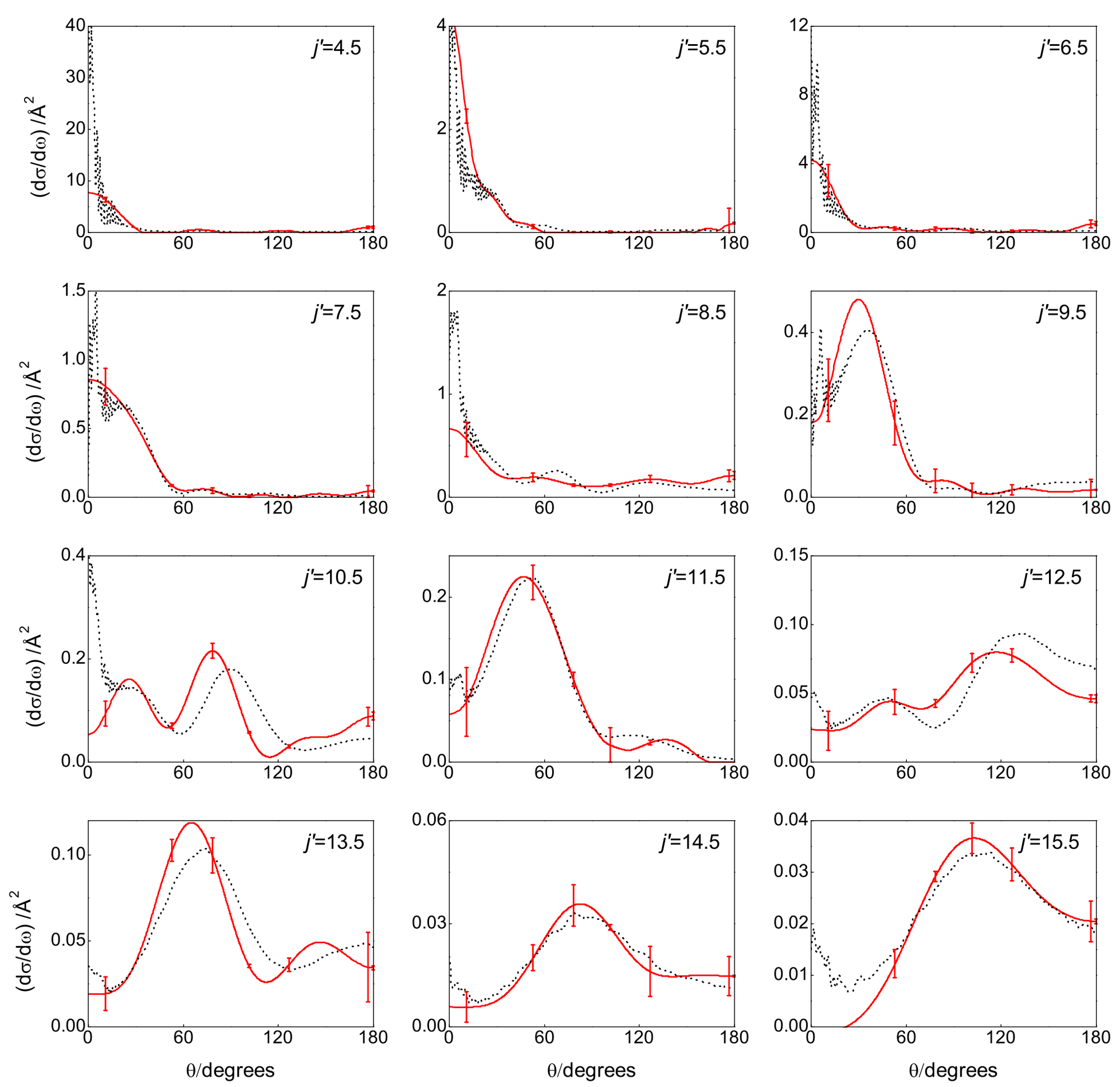
j′=4.5
j′=5.5
j′=6.5
j′=7.5
j′=8.5
j′=9.5
j′=10.5
j′=11.5
j′=12.5
j′=13.5
j′=14.5
j′=15.5
(dσ/dω) /Å²
θ/degrees

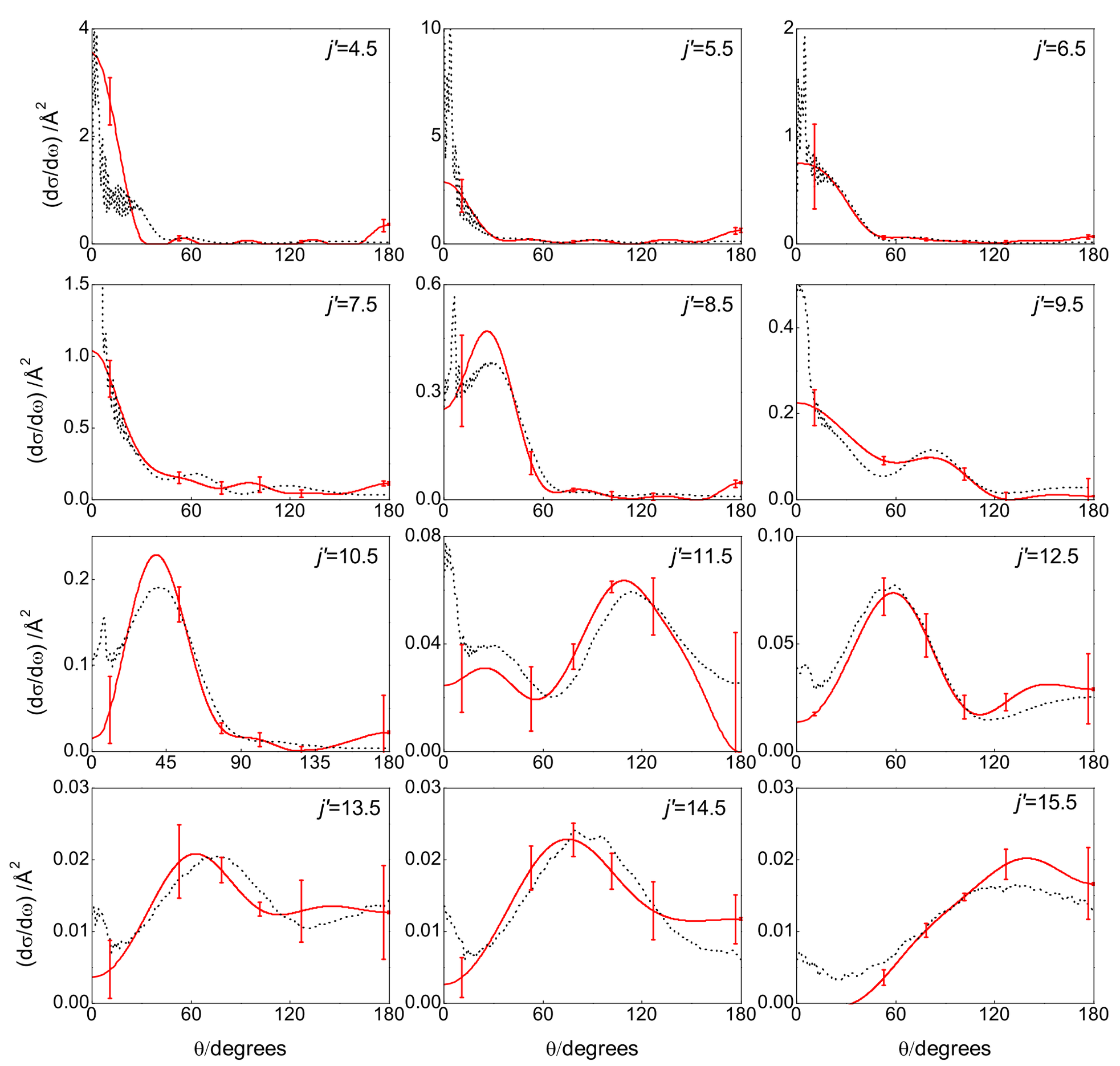
j′=4.5
j′=5.5
j′=6.5
j′=7.5
j′=8.5
j′=9.5
j′=10.5
j′=11.5
j′=12.5
j′=13.5
j′=14.5
j′=15.5
(dσ/dω) /Å²
θ/degrees

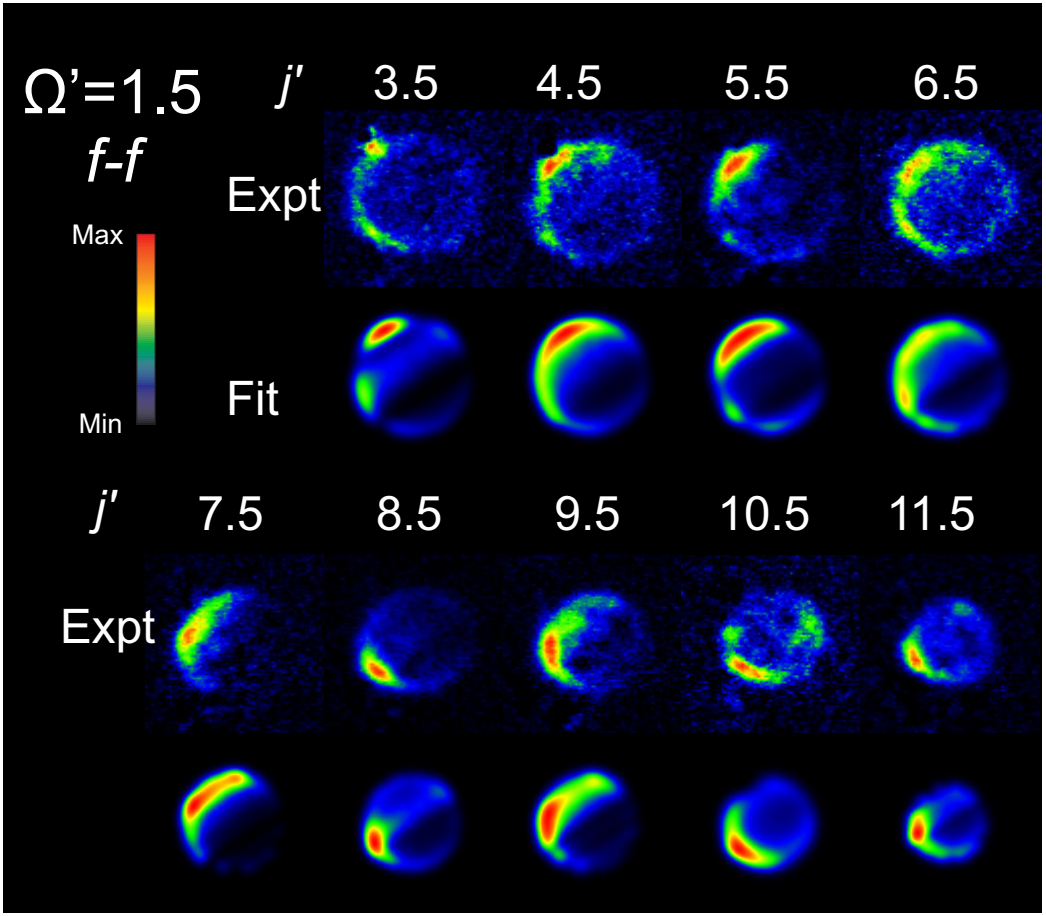
Ω'=1.5
f-f
j'
3.5
4.5
5.5
6.5
Expt
Max
Min
Fit
j'
7.5
8.5
9.5
10.5
11.5
Expt

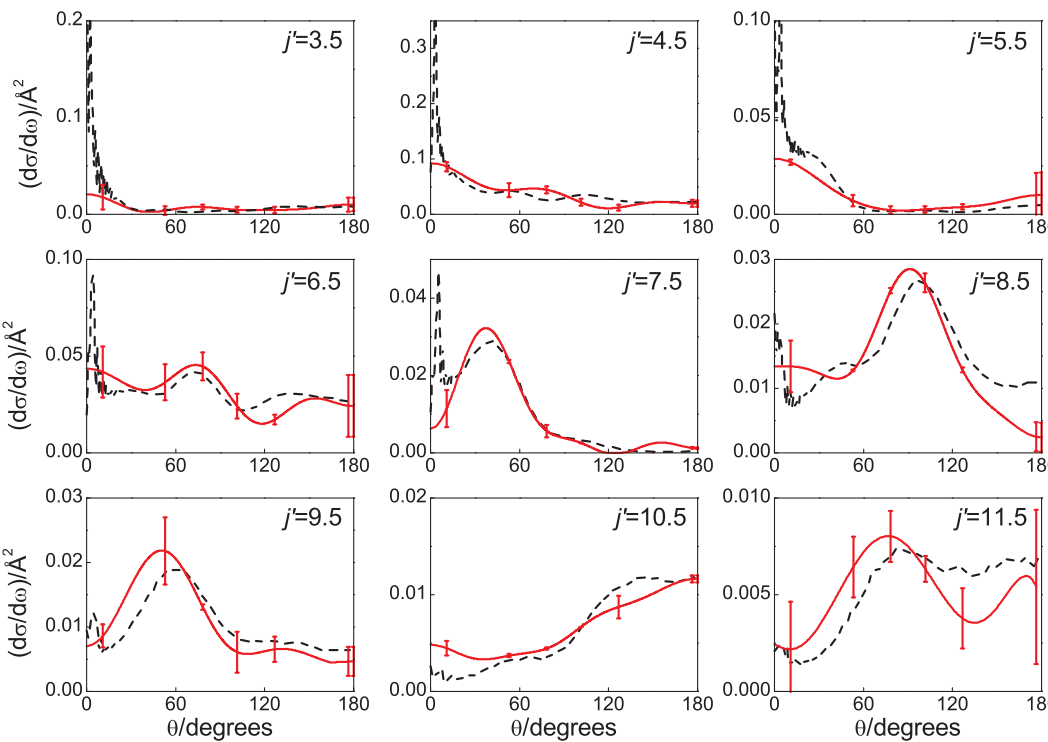
j'=3.5
j'=4.5
j'=5.5
j'=6.5
j'=7.5
j'=8.5
j'=9.5
j'=10.5
j'=11.5
(dσ/dω)/Å²
θ/degrees

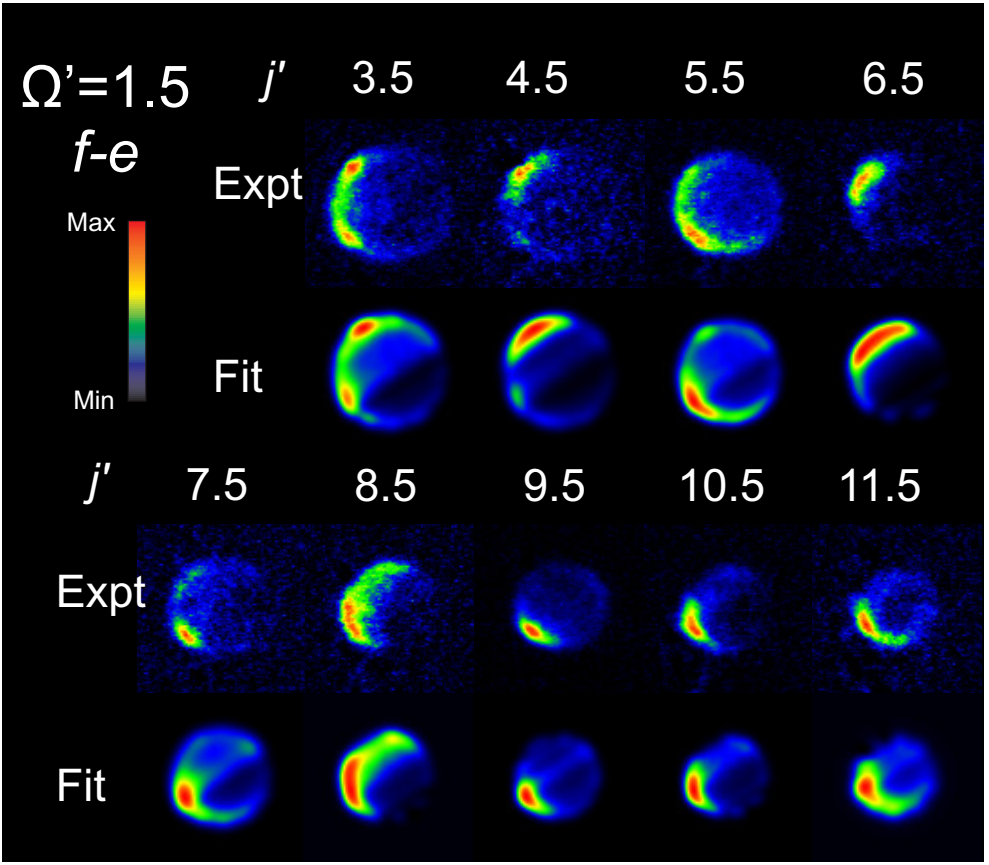
Ω'=1.5
f-e
j'
3.5
4.5
5.5
6.5
Expt
Max
Min
Fit
j'
7.5
8.5
9.5
10.5
11.5
Expt
Fit

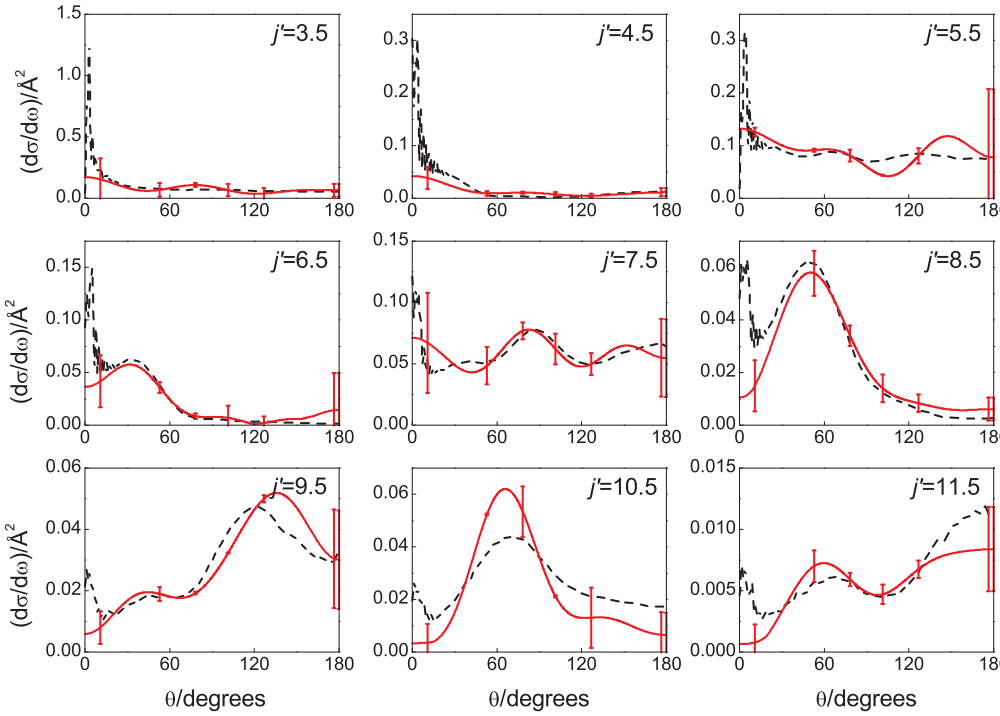
j'=3.5
j'=4.5
j'=5.5
j'=6.5
j'=7.5
j'=8.5
j'=9.5
j'=10.5
j'=11.5
(dσ/dω)/Å²
θ/degrees

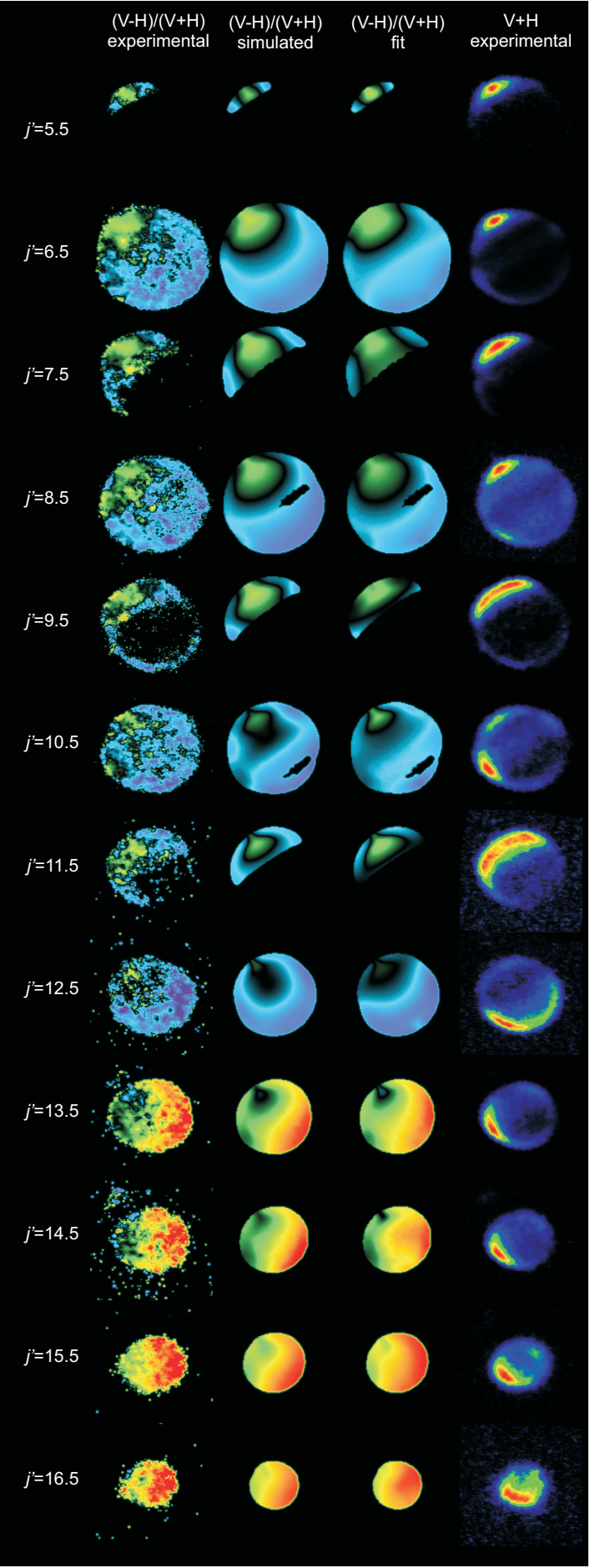
(V-H)/(V+H)
experimental
(V-H)/(V+H)
simulated
(V-H)/(V+H)
fit
V+H
experimental
j'=5.5
j'=6.5
j'=7.5
j'=8.5
j'=9.5
j'=10.5
j'=11.5
j'=12.5
j'=13.5
j'=14.5
j'=15.5
j'=16.5

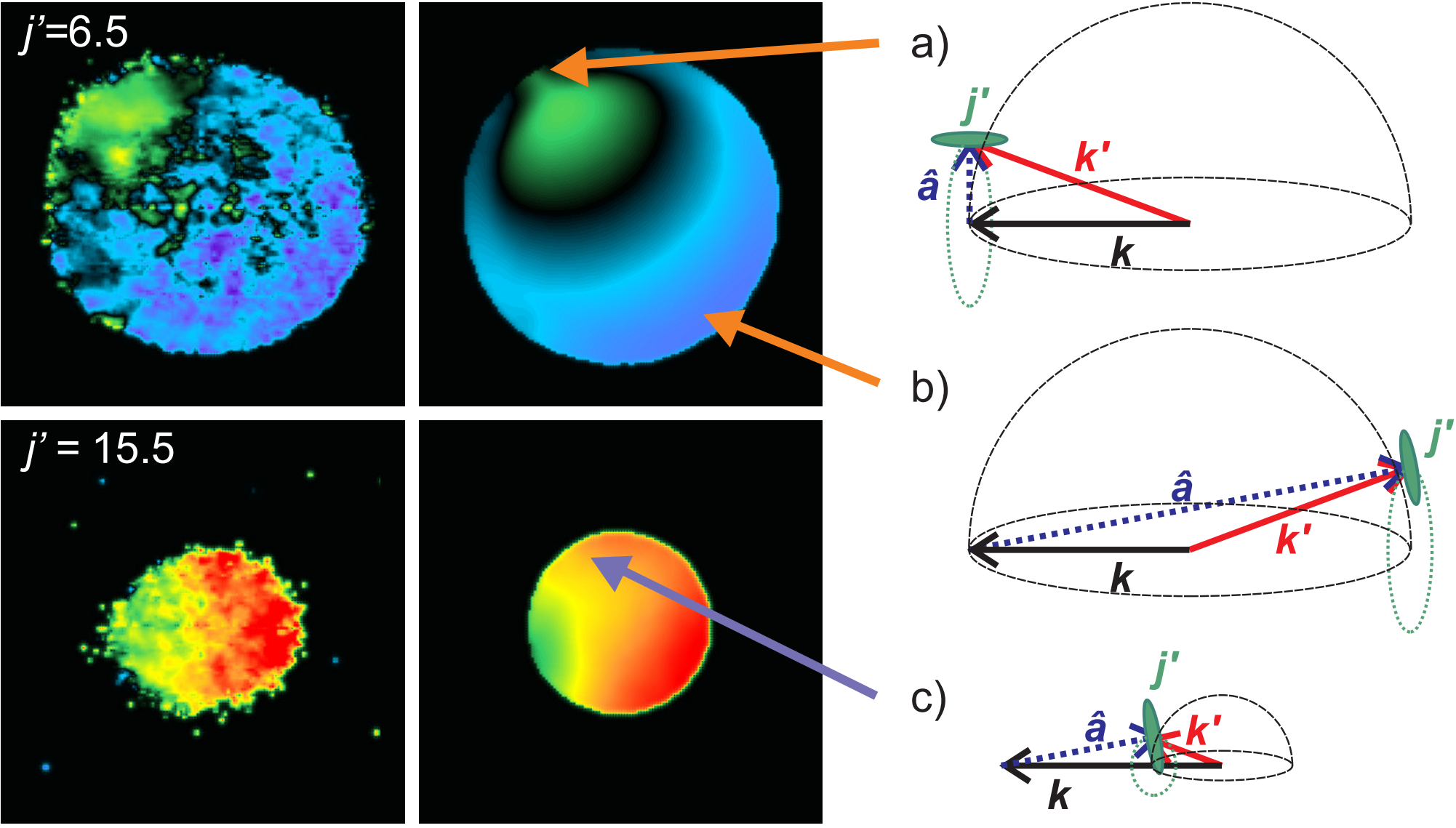
j'=6.5
j' = 15.5
a)
b)
c)
j'
k'
â
k

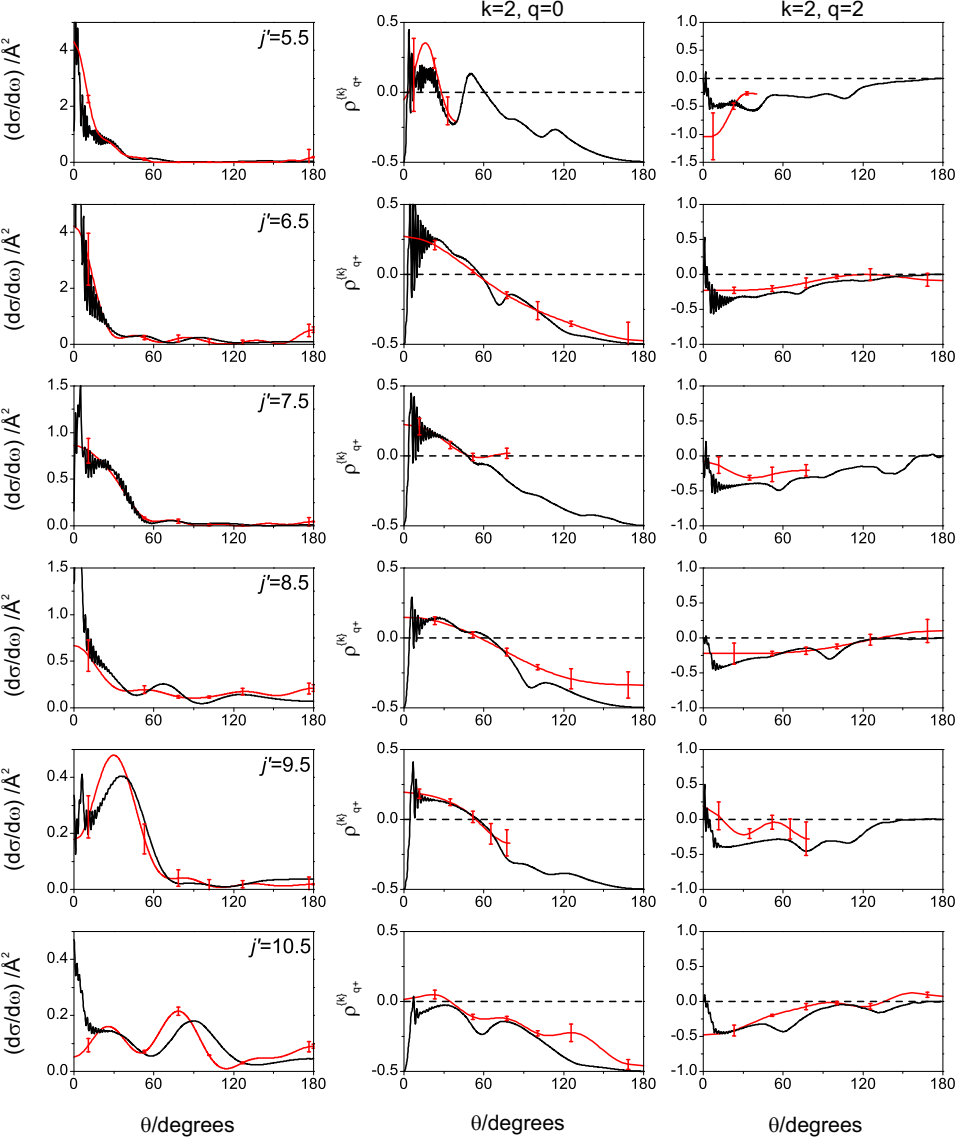
k=2, q=0
k=2, q=2
j'=5.5
j'=6.5
j'=7.5
j'=8.5
j'=9.5
j'=10.5
(dσ/dω) /Å²
ρ(k) q+
θ/degrees

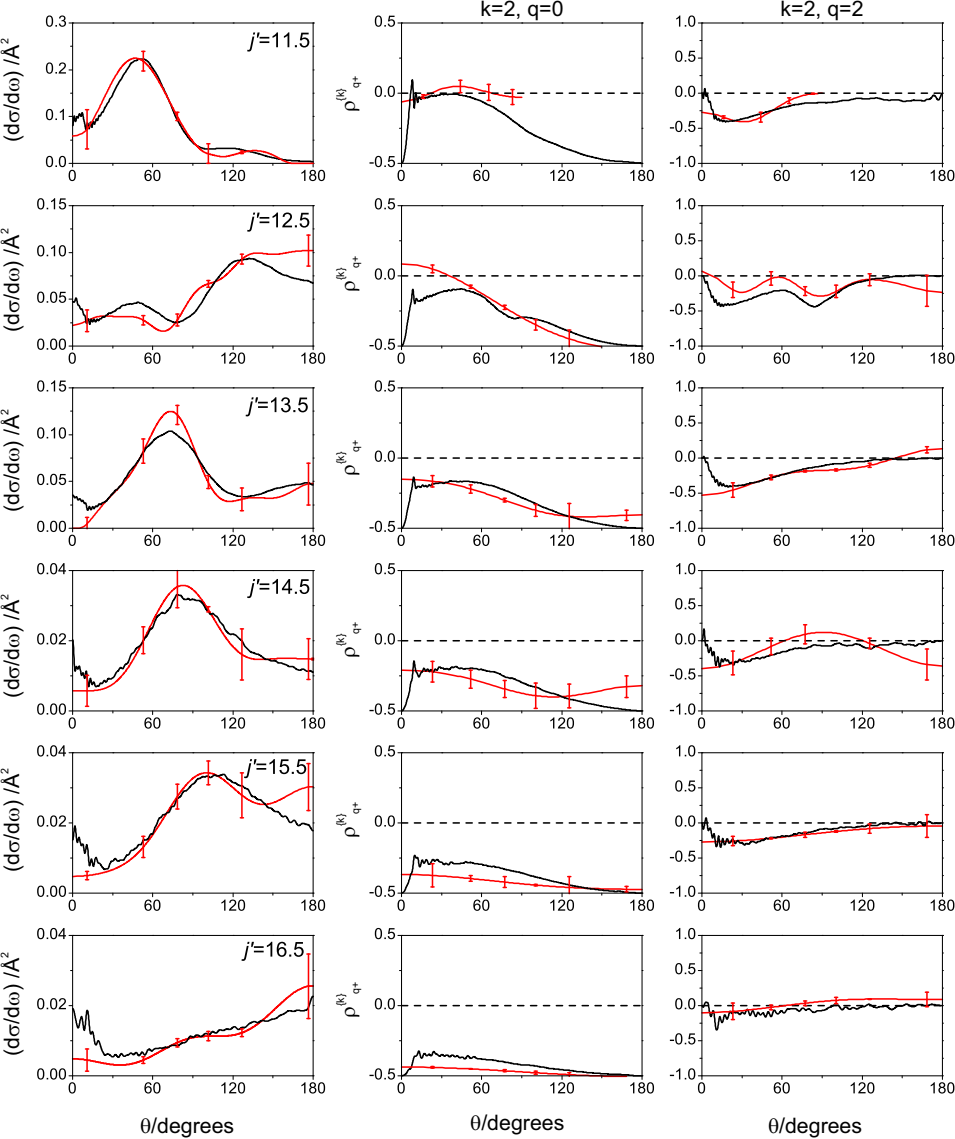
k=2, q=0
k=2, q=2
j'=11.5
j'=12.5
j'=13.5
j'=14.5
j'=15.5
j'=16.5
(dσ/dω) /Å²
ρ(k) q+
θ/degrees

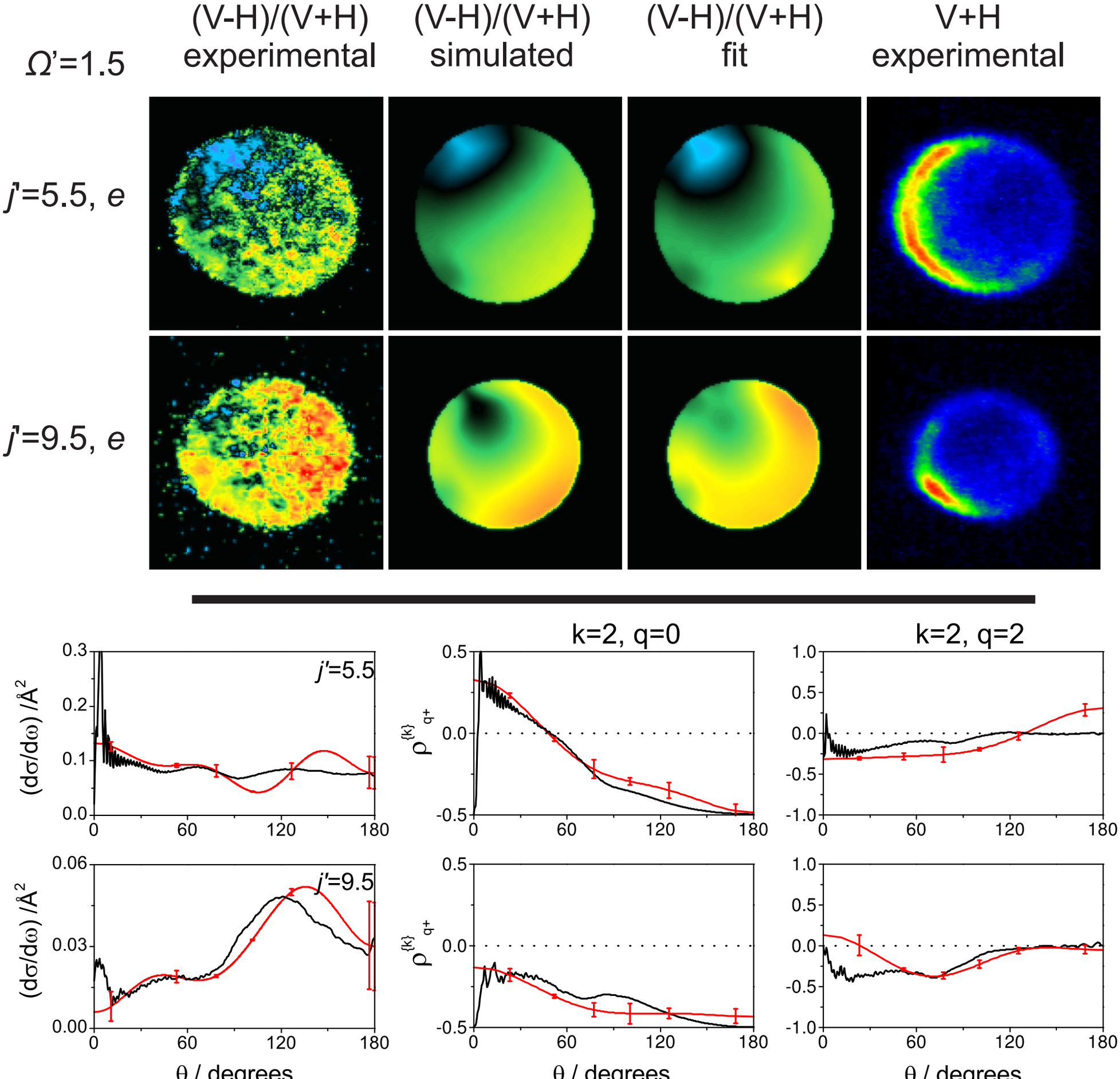
Ω'=1.5
(V-H)/(V+H) experimental
(V-H)/(V+H) simulated
(V-H)/(V+H) fit
V+H experimental
j'=5.5, e
j'=9.5, e
k=2, q=0
k=2, q=2
j'=5.5
j'=9.5
(dσ/dω) /Å²
ρ^{k}_{q+}
θ / degrees

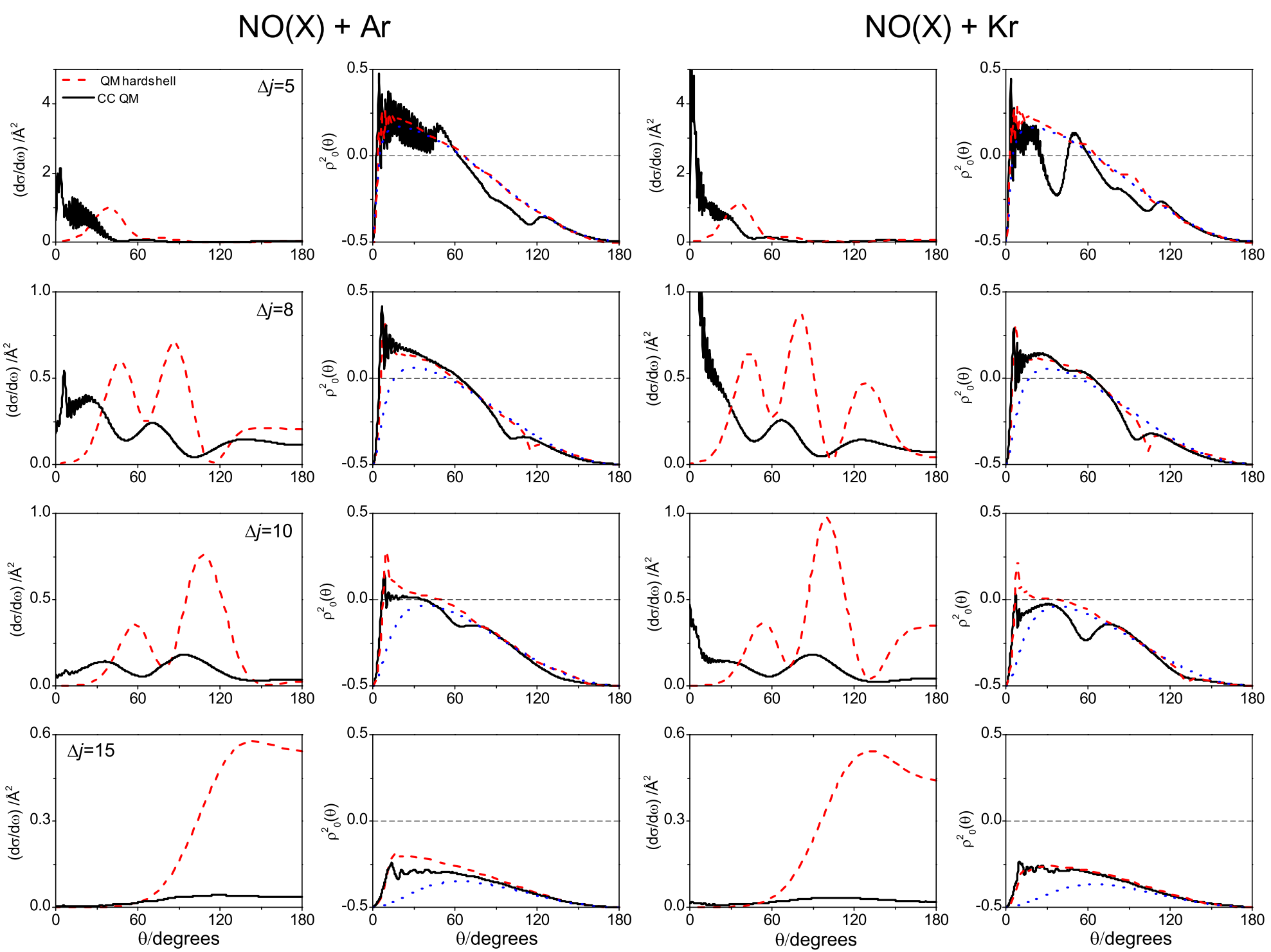
NO(X) + Ar
NO(X) + Kr
QM hardshell
CC QM
Δj=5
Δj=8
Δj=10
Δj=15
(dσ/dω) /Å²
ρ²₀(θ)
θ/degrees